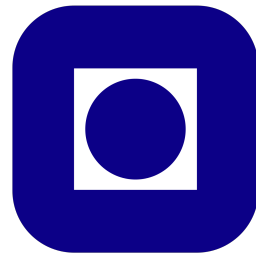

Sources of Ultra High Energy Cosmic Rays and Neutrinos



Henrik Døvle Andrews
Norwegian university of Science and Technology

May 25, 2024

Preface

Lorem ipsum dolor sit amet, consectetuer adipiscing elit. Ut purus elit, vestibulum ut, placerat ac, adipiscing vitae, felis. Curabitur dictum gravida mauris. Nam arcu libero, nonummy eget, consectetuer id, vulputate a, magna. Donec vehicula augue eu neque. Pellentesque habitant morbi tristique senectus et netus et malesuada fames ac turpis egestas. Mauris ut leo. Cras viverra metus rhoncus sem. Nulla et lectus vestibulum urna fringilla ultrices. Phasellus eu tellus sit amet tortor gravida placerat. Integer sapien est, iaculis in, pretium quis, viverra ac, nunc. Praesent eget sem vel leo ultrices bibendum. Aenean faucibus. Morbi dolor nulla, malesuada eu, pulvinar at, mollis ac, nulla. Curabitur auctor semper nulla. Donec varius orci eget risus. Duis nibh mi, congue eu, accumsan eleifend, sagittis quis, diam. Duis eget orci sit amet orci dignissim rutrum.

Abstract

Lorem ipsum dolor sit amet, consectetuer adipiscing elit. Ut purus elit, vestibulum ut, placerat ac, adipiscing vitae, felis. Curabitur dictum gravida mauris. Nam arcu libero, nonummy eget, consectetuer id, vulputate a, magna. Donec vehicula augue eu neque. Pellentesque habitant morbi tristique senectus et netus et malesuada fames ac turpis egestas. Mauris ut leo. Cras viverra metus rhoncus sem. Nulla et lectus vestibulum urna fringilla ultrices. Phasellus eu tellus sit amet tortor gravida placerat. Integer sapien est, iaculis in, pretium quis, viverra ac, nunc. Praesent eget sem vel leo ultrices bibendum. Aenean faucibus. Morbi dolor nulla, malesuada eu, pulvinar at, mollis ac, nulla. Curabitur auctor semper nulla. Donec varius orci eget risus. Duis nibh mi, congue eu, accumsan eleifend, sagittis quis, diam. Duis eget orci sit amet orci dignissim rutrum.

Acknowledgments

I would like to thank my supervisor, Professor Foteini Oikonomou, for her guidance and help throughout this project. I would also like to thank my fellow students for their help and support. Balasubramaniam et al. 2021

Contents

1	Introduction	8
2	The ever-expanding Universe	9
2.1	Cosmological parameters	9
2.2	Shape of the Universe	9
2.3	Redshift	10
2.4	Comoving distance	10
2.5	Luminosity distance	11
3	High Energy Particles	12
3.1	Acceleration of high energy particles	12
3.1.1	The Hillas criterion	13
3.1.2	Macroscopic Acceleration mechanisms	14
3.2	UHECRs	16
3.2.1	Production and Energy loss	16
3.2.2	Detection	16
3.2.3	Emissivity estimates	17
3.3	Neutrinos	18
3.3.1	Production and Energy loss	18
3.3.2	Detection	19
3.3.3	Emissivity estimates	21
4	Probing extra galactic sources	23
4.1	Density and anisotropy	23
4.2	SED broad band analysis	24
4.2.1	X-ray energy budget	25
4.2.2	Radio luminosity	25
4.2.3	Photon fields around AGN	25
4.3	Magnetic field constraints	27
4.3.1	Equipartition	27

4.3.2	Self synchrotron absorption	29
4.3.3	Deviation from SSA and Equipartition	31
4.4	Time-scales analysis	31
5	Active Galactic Nuclei	34
5.1	AGN structure and classification	35
5.1.1	Accretion disk	35
5.1.2	Corona and X-ray emission	37
5.1.3	Broad and narrow line region	37
5.1.4	Dust torus	37
5.1.5	Jets	37
5.2	Types of AGN	38
6	Compact symmetric objects	39
6.1	Sub Classification of CSO	40
6.2	Origin of CSOs/Fueling	42
6.3	Catalogue of Bona fide CSO	43
6.4	Characteristic of CSOs	46
6.5	Prevalence of CSOs	48
7	CSO as sources of UHECRs and neutrinos	49
7.1	Magnetic field strength	49
7.2	Energy budget	51
7.2.1	x-ray power	51
7.2.2	X-ray power	53
7.2.3	Radio power	54
7.2.4	Jet power	54
7.3	Time scales	55
7.4	Composition/Mass Loading	59
7.4.1	Stellar Mass Loading	59
7.4.2	Metallicity	60

7.5 Emissivity of the System	60
7.6 Neutrino Emissivity	61
8 Discussion	62

List of Figures

1	Hillas criterion for proton (blue line) and iron (red line) accelerated up to $10^{20}eV$ and $10^{21}eV$ respectively	13
2	Simulations from Alves, Zrake, and Fiúza 2018 showing the evolution of kink instability in a jet. The upper panels shows the before the KI instability has been amplified, and the lower panel shows the jet after the instability has been amplified. From left to right the panels show, Current density, magnetic field lines, and axial electric field.	15
3	The diffuse flux of UHECRs as measured by the Pierre Auger Observatory and the Telescope Array. The flux is separated into galactic and extra galactic sources where the total spectrum follows the black dots. Image taken from Abdul Halim et al. 2023	18
4	The IceCube neutrino observatory. The detector is located at the South Pole and is a large block of ice instrumented with photomultiplier tubes. Image taken from Andeen and Plum 2019	20
5	The difference between track and cascade events in the IceCube detector. The left image shows a track event where a muon has traveled through the detector. The middle image shows a cascade event where a neutrino has interacted with the ice and produced a shower of particles. The right image shows a double bang event where a tau neutrino has produced a tau lepton which has then decayed. Image taken from Fox 2008	20
6	The diffuse flux of neutrinos as measured by the Ice Cube observatory. The y-axis on the left image is the number of events per bin. The flux is separated into contributions from atmospheric neutrinos and astrophysical neutrinos. The right image is the model astrophysical flux as measured by ICE CUBE. Images taken from Abbasi et al. 2022	22
7	The spectral energy distribution of a typical AGN viewed without interference from the jet. The different components of the AGN are visible in the plot. Image taken from Collinson et al. 2016	24
8	The inverse Compton scattering process. The process is the scattering of a low energy photon by a relativistic electron. The scattered photon will have a higher energy than the original photon. Image taken from Bennun 2020	25
9	The synchrotron spectrum of a Giga hertz peaked galaxy. Later on one will realise that GHP galaxies and CSO occupy that same niche. Image taken from Group of Active Galactic Nuclei investigation at https://www.sao.ru/hq/giag/gps-en.html	29
10	Schematic view of the radiative transfer in a spherical ball of plasma. Image taken from Hirotani 2005	31
11	Pion resonance cross section, and the inelasticity of the interaction. Image taken from C. D. Dermer and Menon 2009	33
12	AGN unification	36
13	The radio structure of CSO J0741+2706. The core is determined from the flat spectrum component and the symmetry of the radio lobes. Image taken from Tremblay et al. 2016 . . .	40
14	The different phases of CSO 2 sources. Image taken from Sullivan et al. 2024	41
15	Distribution of redshift of different classes	46
16	The radio luminosity at peak frequency of CSOs as a function of linear size.	47

17	The radio luminosity at peak frequency of CSOs as a function of redshift.	47
18	Magnetic field strength estimated from the equipartition method. The errorbars are calculated from the span of values obtained from different spectral index ranging from 0.6 to 1.3.	50
19	Magnetic field strength estimated from the SSA method. The errorbars are calculated from the span of values of $b(\alpha)$ obtained from different optical thickness. $b(\alpha)$ ranges from 1.08 to 2.38.	50
20	Hillas diagram for the CSO. The red line represents the maximum energy of the proton that can be accelerated in the system, and blue is the same just for Iron.	52
22	Jet power of the CSOs in table 3. The jet power is calculated using the minimum jet power argument based on magnetic field equipartition. The bars in line with each line represent the estimated jet power based on the X-ray luminosity varying the value of α in equation 70. . .	56
23	SED of the different regions in the CSO. The SED is based on the parameters in table 7. . .	57
24	Characteristic timescales for the CSO. Processes included is synchrotron losses and photopion losses. The timescales are calculated for a spherical size of $R_{\text{lobe}} = 2pc$ and a magnetic field strength of $B = 10^{-2}G$. The photon field is based on the parameters in table 7.	58
25	Schematic of the shock in the CSO. The shock is created by the expansion of the lobes into the ambient medium through jet pressure. Image taken from Perucho and Marti 2002	59

List of Tables

1	The model parameters for the astrophysical flux of UHECRs as measured by the Pierre Auger Observatory and the Telescope Array.	17
2	The model parameters for the astrophysical flux of neutrinos as measured by the Ice Cube observatory.	21
3	Catalogue of bona fide CSOs. Data taken from Kiehlmann, Lister, et al. 2023	44
4	Classification of CSOs in the catalogue.	45
5	Overlapping sources between the NRAO catalogue and Kiehlmann, Lister, et al. 2023 and the extracted values scaled to represent one lobe hotspot.	49
6	X-ray flux of the CSOs in table 3 found in the data set in Wójtowicz et al. 2020. The X-flux is given in units of 10^{42} erg/s.	53
7	Parameters used to determine the SED of the different regions.	58
8	Mass Loading and Extra-Galactic Results for Different Species	61

1 Introduction

1. The motivation for looking for UHECRs and Neutrinos
2. What multimessenger astronomy can give us
3. The difficulty of knowing the sources of multimessengers
4. The possible source population
5. Outline

2 The ever-expanding Universe

To investigate sources very far away from an observer it is important to understand the influence this distance has on the desired observables. Therefore, in astrophysics and astronomy in general there are distances created to take into account the effects of an expanding Universe. This chapter draws heavily from Hogg 2000.

2.1 Cosmological parameters

A reasonable place to start is with the Hubble constant H_0 . This parameter sets the recession speed of a point at proper distance d and the current position via the relation $v = H_0 d$. The subscript 0 refers to the present epoch signifying that H_0 is not static but changes with time. The precise value of H_0 is quite debated, so it's commonly expressed in a parameterised form,

$$H_0 = 100 \frac{\text{km}}{\text{s}} \frac{1}{\text{Mpc}} h.$$

The parameter h is a dimensionless number that according to current knowledge can take the value between 0.5 to 0.8 reflecting the range of answers collected from recent work.

Beyond its basic definition, H_0 also allows for the derivation of two significant cosmic scales:

Hubble Time (t_H) : Defined as the inverse of H_0 , t_H provides an estimate of the age of the Universe. It sets a scale for the time since the Big Bang, assuming the Universe has been expanding at a constant rate. The equation $t_H = 1/H_0 \approx 14$ Billion years offers a way to approximate this expansion timescale.

Hubble Distance (D_H) : This is a measure of the distance. Calculated as $D_H = c/H_0 \approx 4.4$ Gly, where c is the speed of light, it represents a critical boundary in observational cosmology.

2.2 Shape of the Universe

The shape and expansion of the Universe are central themes in cosmology, but to model such one needs to define the structure of the Universe and its contents. In this report and many articles, the Universe is often explored through the lens of the flat Lambda Cold Dark Matter (Λ CDM) model. This model, widely accepted in contemporary cosmology, provides a framework for understanding the Universe's composition and its expansion dynamics by assuming as the name suggests no curvature and cold dark matter. In the Λ CDM model, two key parameters are important: the mass density of the Universe, ρ_0 , and the cosmological constant, Λ . These parameters, which evolve, are a part of defining the metric tensor in general relativity, thereby allowing us to model the curvature of the Universe based on its initial conditions. These parameters are often expressed as dimensionless variables:

$$\Omega_m = \frac{8\pi G \rho_0}{3H_0^2}$$

$$\Omega_\Lambda = \frac{\Lambda c^2}{3H_0^2}$$

Here, Ω_m represents the matter density parameter, encompassing both ordinary (baryonic) matter and dark matter. Ω_Λ , on the other hand, corresponds to the density parameter associated with the cosmological constant, which is often interpreted as dark energy.

In general, one has a third density parameter Ω_k which defines the curvature of space-time and the relationship between these parameters is expressed as:

$$\Omega_m + \Omega_\Lambda + \Omega_k = 1$$

In a flat Universe, one has $\Omega_k = 0$ and the Universe is dominated by dark energy and dark matter. The model used in this report and the papers used in the following chapters is the flat Λ CDM model where the parameters take the values of $\Omega_\Lambda = 0.7$ and $\Omega_m = 0.3$. These values align with current observational data.

2.3 Redshift

Redshift is defined as the fractional Doppler shift of emitting light. The Doppler effect is a known effect on different observables in the Universe where the relative motion of sources to observers will impact the observable. The redshift is quantified for a light source as

$$z = \frac{\nu_e}{\nu_o} - 1 = \frac{\lambda_o}{\lambda_e} - 1 \quad (1)$$

Here o refers to the observed quantity and e the emitted. Due to the expansion of the Universe the light emitted from a distant source will be increasingly redshifted the further away it is. In these scenarios the redshift serves as a distance measure, allowing us to deduce distances to faraway objects.

2.4 Comoving distance

Comoving distance is an important concept in cosmography, acting as a standard unit for various distance measurements in the Universe. This distance, often termed the line-of-sight distance for an observer on Earth, remains constant even as objects expand with the Hubble flow. To calculate the total comoving distance (D_c) to an object, one integrates the differential comoving distances (δD_c) along the line of sight, starting from redshift $z = 0$ to the object. This integration necessitates consideration of the Universe's parametric composition and the δD_c is expressed as

$$\delta D_c = \frac{D_H}{E(z)} dz, \quad (2)$$

where the function $E(z)$ is defined as

$$E(z) = \sqrt{\Omega_m(z+1)^3 + \Omega_k(1+z)^2 + \Omega_\Lambda}. \quad (3)$$

Here, $E(z)$ incorporates the density parameters previously discussed and the redshift z . It also relates to the Hubble constant observed by a hypothetical observer at redshift z , expressed as $H(z) = H_0 E(z)$.

One then calculates the comoving distance D_c from

$$D_c = D_H \int_0^z \frac{dz}{E(z)} \quad (4)$$

In addition to the line of sight, one can define the transverse comoving distance D_m . This distance relates two points in the night sky at the same redshift separated by an angle $d\theta$. The actual distance between them $d\theta D_m$ will then vary depending on the curvature of the Universe. This relationship is summarized in

the following equation which accounts for different geometries,

$$D_m = \begin{cases} D_h \frac{1}{\sqrt{\Omega_k}} \sinh\left(\frac{\sqrt{\Omega_k} D_c}{D_H}\right) & \text{if } \Omega_k > 0 \\ D_c & \text{if } \Omega_k = 0 \\ D_h \frac{1}{\sqrt{|\Omega_k|}} \sin\left(\frac{\sqrt{|\Omega_k|} D_c}{D_H}\right) & \text{if } \Omega_k < 0 \end{cases}$$

The different cases correspond to hyperbolic, flat, and spherical geometry respectively. The true nature of the Universe is still unknown, but recent observations indicate a flat Universe.

2.5 Luminosity distance

The luminosity distance D_l is defined through the relation between the bolometric flux F of a source and its bolometric luminosity L . Bolometric flux is the energy received per unit of time per unit area without any obscuration, while bolometric luminosity is the total energy emitted per unit of time. The luminosity distance is defined as

$$D_l = \sqrt{\frac{L}{4\pi F}} \quad (5)$$

It is related to the transverse comoving distance via

$$D_l = (1+z)D_m. \quad (6)$$

If one wants to calculate the spectral flux/ differential flux one needs to take into account a correction. This correction comes from the fact that one is viewing a redshifted object. The object is emitting in a different band than observed. The spectrum of the differential flux F_ν is related to the spectral luminosity via

$$F_\nu = (1+z) \frac{L_{(1+z)\nu}}{L_\nu} \frac{L_\nu}{4\pi D_l^2}. \quad (7)$$

All these equations listed help include the effects of an expanding Universe when astronomers study distant objects and their properties.

3 High Energy Particles

1. Introduction to high energy particles, cosmic rays, and neutrinos. The standard model.
2. The acceleration mechanisms of cosmic rays and neutrinos., derive the power of a particle undergoing first order Fermi acceleration.
 - (a) The Hillas criterion
 - (b) Derive the power of a particle undergoing first order Fermi acceleration.
 - (c) Timescales for acceleration
3. Talk about the nature of Cosmic rays
 - (a) The composition of cosmic rays
 - (b) Energy loss mechanisms of cosmic rays
 - i. Photopion production
 - ii. Synchrotron radiation
 - iii. GZK cutoff
 - iv. Pair production
 - v. local volume limit due to these losses
 - (c) Detection
 - i. Detectors and retracing
 - ii. Emissivity of local volume
 - iii. Spectrum
4. Neutrinoes
 - (a) Production
 - (b) Flavour mixing
 - (c) Energy loss mechanism
 - (d) Detection
 - i. detectors and difficultu of detection
 - ii. retracing
 - iii. Emissivity of local volume?
 - iv. Spectrum

In this section one will define and discuss the nature of high energy particles such as high energy cosmic rays(UHECRS) and neutrinos.

3.1 Acceleration of high energy particles

Acceleration of high energy particles is still a complicated problem in astrophysics and there are still many open questions. The main ways of acceleration are through shocks, magnetic reconnection, and one-shot acceleration, and one will go through to varying degree these methods in this section.

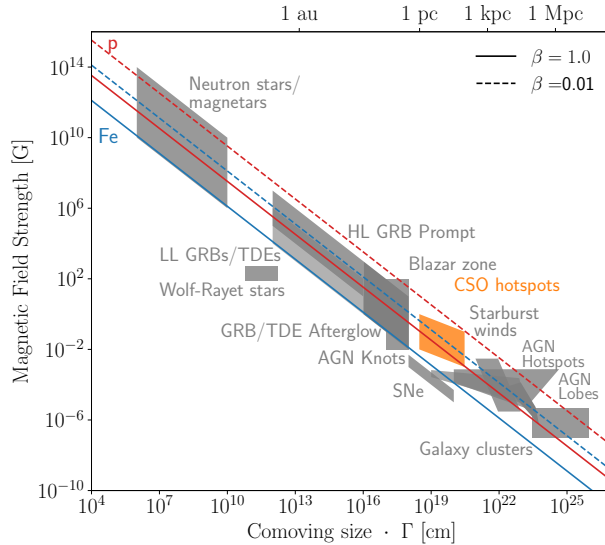


Figure 1: Hillas criterion for proton (blue line) and iron (red line) accelerated up to $10^{20}eV$ and $10^{21}eV$ respectively

3.1.1 The Hillas criterion

Before one delves into macroscopic acceleration models one can start with a bigger picture. By arguing that the acceleration, whatever it may be, needs to be of a certain strength and that the particle being accelerated needs to stay confined within the accelerating region for long enough one can create an upper band on the maximum energy reach by charged particle. This simple but powerful criterion is called the Hillas criterion introduced in Hillas 1984, and is a way of estimating the maximum energy a particle can reach in a given source for a given uniform magnetic field.

For relativistic particles with charge Z and energy ϵ in a magnetic field of strength B one can define the Larmor radius

$$R_L = \frac{\epsilon}{ZB} \quad (8)$$

By arguing that the confinement of a particle to an accelerating region is the same as setting the Larmor radius equal to the size of the source, one can easily derive the maximum achievable energy for a particle as follows;

$$\epsilon_{max} = ZBR \quad (9)$$

Via this method, one can estimate the potential candidates that can produce the observed high-energy particles. The criterion works as an upper boundary of acceleration sources since it does not account for energy loss in the acceleration process or any type of interaction that one could expect to be in turbulent environments. In figure 1 one can see the different candidates for the acceleration of two different ions, protons, and iron. One of the candidates is the AGN, which is the focus of this paper.

3.1.2 Macroscopic Acceleration mechanisms

In order to accelerate particles to high energies, one needs to have a mechanism that can transfer energy to the particles. This usually happens through electromagnetic fields, and there are several ways this is thought to happen.

One-shot acceleration: The simplest yet still a powerful way of accelerating particles is through what is called one-shot acceleration. In the presence of an ordered electromagnetic fields, one can continuously accelerate charged particles which will follow the field lines. This can be induced from a rotating magnetic field or a straight electric field, all which create an electromagnetic force on a hypothetical charged particle. This could be the feature of some astrophysical objects such as neutron stars and black holes, usually in a quite close proximity to the object in question.

Second order Fermi acceleration/Diffusive acceleration In regions where one has high variability in the magnetic field strength, one can accelerate particles via scattering. The idea is that charged particles scatter on what can be seen as magnetic clouds and gain energy in the process due to the speed of the clouds. This mechanism is dubbed second order fermi acceleration due to the average energy gain of a particle being proportional to $(\frac{v}{c})^2$. Here v is the speed of the cloud and c is the speed of the particle. This is a slow process due to the proportionality to v^2 , but as mentioned in C. Dermer 2001 can be a viable way of accelerating particles which already have a high energy. In modern times the magnetic mirrors that particles scatter on are thought to be plasma waves. The idea is that particles occupy a background magnetic field B_0 with a superimposed fluctuating electromagnetic field which arises due to cold-plasma waves. The full formalism is described in C. D. Dermer and Menon 2009 at page 361. In trying to shorten the explanation on only focuses on the resulting energy gain. The mean rate of change of the momentum of a particle is given as

$$\left\langle \frac{dp}{dt} \right\rangle = \frac{1}{p^2} \frac{\partial}{\partial p} [p^2 D(p)] \quad (10)$$

where the real challenge lies in determining the diffusion coefficient $D(p)$ which is a function of the particle momentum and pitch angle. One will follow the approach found in O'Sullivan, Reville, and Taylor 2009 in which one only considers Alfvén waves which take a one-dimensional power spectrum $W(k) \propto k^{-q}$, where q is the spectral index and the total internal energy of the waves is given as $\frac{\delta B^2}{8\pi} = \int_{k_{min}}^{k_{max}} W(k) dk$.

As given in O'Sullivan, Reville, and Taylor 2009 the diffusion coefficient with current wave spectrum can be given as

$$D(p) = \beta_a^2 \frac{\delta B^2}{B_0^2} \left(\frac{r_g}{\lambda_{max}} \right)^{q-1} \frac{p^2 c^2}{r_g c} \quad (11)$$

where $\beta_a = \frac{B}{\sqrt{4\pi n_p m_p c}}$ is the Alfvén speed, $r_g = \frac{pc}{ZeB}$ is the gyroradius of the particle, and λ_{max} is the maximum wavelength of the waves, which will be specified when necessary, but if one is following O'Sullivan, Reville, and Taylor 2009 takes the value of $0.1R$, i.e. a magnitude lower than the radius of the emitting region.

From here one can estimate the acceleration timescale of a particle in a given region. The timescale is given as

$$t_{acc} = \frac{p^2}{D(p)} \quad (12)$$

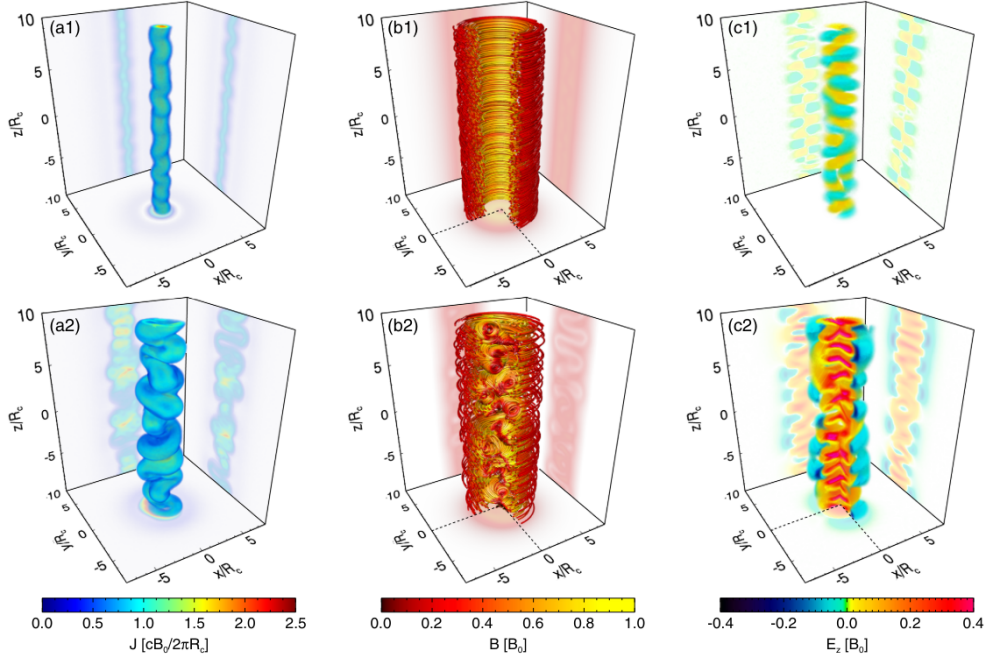


Figure 2: Simulations from Alves, Zrake, and Fiuza 2018 showing the evolution of kink instability in a jet. The upper panels shows the before the KI instability has been amplified, and the lower panel shows the jet after the instability has been amplified. From left to right the panels show, Current density, magnetic field lines, and axial electric field.

First order Fermi acceleration In regions where one has strong shock fronts, one can accelerate particles to high energies. These environments can be found several places where the interstellar medium is interacting with a powerful source of energy. One of the most famous examples of this is the supernova remnant where one sees a powerful shock front as a result of a supernova explosion. The first-order Fermi acceleration happens when particles traverse these strong shock fronts, and when a particle moves through the shock it gains energy proportional to $\frac{v}{c}$. In addition to this, there is a probability that the particle will stay in the accelerating region and experience several accelerations.

In C. Dermer 2001 they can derive the relative power of a particle undergoing first-order Fermi acceleration in a relativistic shock, and it is given as

$$\dot{p} = \frac{2p}{t_u} = \frac{2cqB\Gamma}{mc^2} \quad (13)$$

where t_u is the time in the upstream frame, p is the momentum of the particle, c is the speed of light, q is the charge of the particle, B is the magnetic field strength, Γ is the Lorentz factor of the shock, and m is the mass of the particle.

Kink instabilities(KI) in jets Another method of acceleration which really is diffusive one shot acceleration related to AGN jets is acceleration via the kink instability in jets. The explanation of kink instability leading to acceleration is found in Alves, Zrake, and Fiuza 2018. Kink instability is a hydrodynamic instability that arises in jets when the magnetic field is not aligned with the jet. If a perturbation is introduced to the jet, the resulting force on the jet structure will magnify the perturbation. This will lead the jet to a much more complicated structure, and twist the magnetic field lines. See figure 2 for an illustration. The paper argues that a highly tangled magnetic field and a large scale inductive electric field which is found throughout the kink-unstable region will lead to rapid energization of particles.

3.2 UHECRs

UHECRs are charged particles that are bombarding the Earth with energy exceeding 1 exaelectronvolt (10^{18} eV) according to Alves Batista et al. 2019. The exact origin of these particles is still a mystery but due to their high energies, they are thought to be extragalactic. The composition of UHECRs ranges from protons to heavier nuclei such as helium or iron, and when these particles interact with the atmosphere they produce a shower of secondary particles. The air showers can contain a lot of information such as energy and direction, and through the use of large detectors, one can reconstruct the original cosmic ray and the spectra of UHECRs. In this section, I will discuss the nature of UHECRs, their energy loss mechanisms, and how they are detected.

3.2.1 Production and Energy loss

The requirements to produce a UHECR are a charged particle and a powerful accelerator. During a particles acceleration and after it has escaped there are several ways a particle can lose energy. In order to model them sufficiently one needs to take into account these energy loss mechanisms in their journey to Earth.

The important parameters for this energy loss are its composition and its environment. In addition to energy, the interstellar magnetic field will also deflect the particles and therefore the direction of the particle will be changed during its propagation. What these effects can show us is that all UHECRs have a finite distance they can travel before they lose too much energy and therefore the volume in which they can be produced is limited. Here I will briefly discuss the most important energy loss mechanisms.

Photo-pair production

$$p + \gamma \rightarrow p + e^- + e^+ \quad (14)$$

For UHECRs, the most dominant sink of energy when under a certain energy threshold is the Bethe-Heitler process. In this process, a proton of sufficient energy interacts with the photon field in its vicinity and produces a pair of electrons and positrons. The photon field can vary from the cosmic microwave background to the generated field from different sources. The energy loss of this process is quite small $\sim \frac{2m_e}{m_p} = 10^{-3}$ of the original energy of the proton, but the process is very common, and therefore it is a significant energy loss over time.

Photo-Pion production

$$p + \gamma \rightarrow \Delta^+ \rightarrow (p + \pi^0) \quad \text{or} \quad (\pi^+ + n) \quad (15)$$

Given enough energy the proton can interact with a photon field and produce a delta resonance. This resonance can then decay into a pion and a proton or a pion and a neutron. In this mechanism the original proton loses $m_p/m_\pi \approx 20\%$ of its energy resulting in a quite rapid loss of energy. This mechanisms is important since it also puts an upper limit on the UHECR energy for intergalactic particles. This limit, called the Greisen-Zatsepin-Kuzmin (GZK) limit comes from the UHECRs interacting with the cosmic microwave background in this delta resonance process. The limit caps proton energy at 5×10^{19} eV.

3.2.2 Detection

When a high-energy cosmic ray hits the Earth's atmosphere, it sets off a cascade of interactions with air molecules, resulting in the emission of secondary particles and light. Detecting this cascade is much more feasible than capturing the original cosmic ray itself.

J_0	E_{ank}	γ_1	γ_2	γ_d	E_s
3.3×10^{-19}	4.82×10^{18}	3.14	4.2	3.14	4.2×10^{19}

Table 1: The model parameters for the astrophysical flux of UHECRs as measured by the Pierre Auger Observatory and the Telescope Array.

In addition, since the UHECR flux at high energy is extremely low (< 1 particle per km^2 per year for $E > 10^{19}$) one needs a large area to collect enough events. The largest UHECRs detectors of present are the Pierre Auger Observatory and the Telescope Array.

The Pierre Auger Observatory is located in Argentina and is the largest detector of its kind. It consists of 1660 Cherenkov detectors spread over 3000 km^2 and 27 fluorescence telescopes in four locations. With these instruments, the observatory is very capable of reconstructing the air showers and therefore the energy and direction of the cosmic ray. The observatory has a blind spot in the night sky and therefore the observatory is complemented by the Telescope Array located in Utah. The Telescope Array is a smaller observatory with 507 scintillator detectors and 3 fluorescence telescopes. Combined they have been able to map the full sky of UHECRs.

When a cosmic ray interacts with the atmosphere it produces a shower of secondary particles. These particles will then interact with several of the Cherenkov detectors located on the ground at approximately the same time. By measuring the time difference between the detectors one can reconstruct the direction of the cosmic ray. The energy of the cosmic ray can also be reconstructed by combining the measurements from the Cherenkov detectors. There is also a secondary detector in the Pierre Auger Observatory called the fluorescence detector. This detector will make use of the very faint glow that the air shower produces when it interacts with particles in the atmosphere. The detector will then observe a shower as a trace of light in the sky and by measuring the total amount of light one can infer the energy, while the shape of the trace can give naturally the direction of the cosmic ray.

3.2.3 Emissivity estimates

From the detectors on earth great strides have been made in modeling the flux of UHECRs. The flux is modeled as a power law and the model parameters are taken from Collaboration et al. 2017 and are shown in table 1. The flux is thought to be separated into contributions from extragalactic sources and galactic sources, and with this information one can start to make tangible estimates of the sources of UHECRs. One such estimate is the emissivity of UHECR sources. The emissivity is a measure of the energy released per unit time per unit volume. The question one can ask is what is the necessary emissivity of UHECRs to explain the observed flux here on Earth? In other words, what is the required energy injection rate per unit volume of UHECRs?

$$J(E_v) = \begin{cases} J_0 \left(\frac{E_v}{E_{\text{ank}}} \right)^{-\gamma_1} & \text{if } E_v < E_{\text{ank}} \\ J_0 \left(\frac{E_v}{E_{\text{ank}}} \right)^{-\gamma_2} \left(1 + \left(\frac{E_{\text{ank}}}{E_s} \right)^{\gamma_d} \right) \left(1 + \left(\frac{E_v}{E_s} \right)^{\gamma_d} \right)^{-1} & \text{if } E_v \geq E_{\text{ank}} \end{cases} \quad (16)$$

By separating the flux into contributions from extragalactic sources and galactic sources one can estimate the observed energy density in the Universe of extragalactic UHECRs ρ_{UHECR} . Subsequently, one can define an energy loss time for a UHECR as the loss length divided by the speed of light c . The loss length is a measure of the distance a UHECR can travel before its energy drops below a certain threshold, and for our simple analysis, we will use the length of $1Gpc$. This number is comparable in magnitude as found by Stanev 2009, but as the loss length is dependent on initial energy and composition our number will be an approximation.

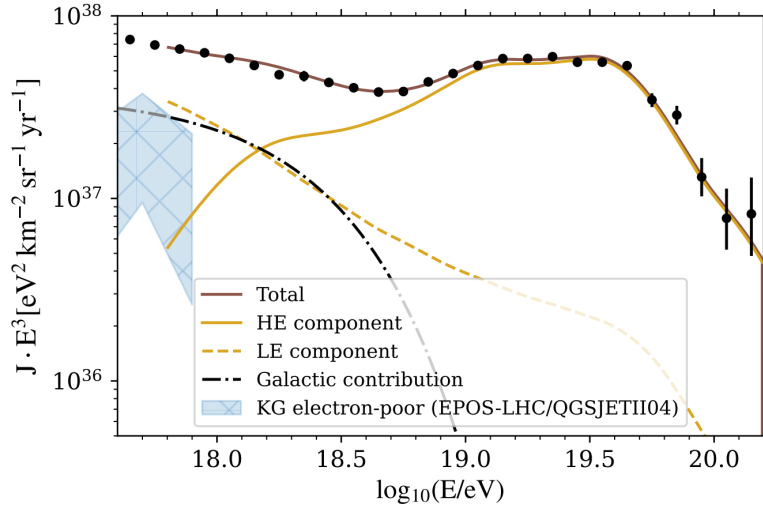


Figure 3: The diffuse flux of UHECRs as measured by the Pierre Auger Observatory and the Telescope Array. The flux is separated into galactic and extra galactic sources where the total spectrum follows the black dots. Image taken from Abdul Halim et al. 2023

The emissivity of UHECRs is then given as

$$\epsilon_{\text{UHECR}} = \frac{u_{\text{UHECR}}}{t_{\text{loss}}} = \frac{u_{\text{UHECR}}}{D_{\text{loss}}/c} = \frac{4\pi c \int_{E_0}^{E_{\max}} J_{\text{extragalactic}}(E) EdE}{c D_{\text{loss}}} \quad (17)$$

Here u_{UHECR} represents the energy density of extragalactic UHECRs, t_{loss} is the energy loss time, D_{loss} is the loss distance, $J(E)$ is the flux of UHECRs, $E_0 = 1$ exaelectronvolt, is the minimum energy of the flux where extragalactic UHECRs become important, and E_{\max} is the maximum energy of extragalactic UHECRs. By using the parameter value in table 1 for the UHECRs flux one receives the value of $9 \times 10^{44} \frac{\text{erg}}{\text{Mpc}^3 \text{yr}}$ for the emissivity of UHECRs. This emissivity is a crude estimation of the required energy injection rate of UHECRs and is meant to give a rough estimate. This is comparable to a more thorough analysis from Aab et al. 2020 which received a value of $6 \times 10^{44} \frac{\text{erg}}{\text{Mpc}^3 \text{yr}}$.

3.3 Neutrinos

The second particle of interest is the neutrino. Neutrinos compared to UHECRs are neutral particles that are produced in various processes in the Universe. The most common and well-known is the fusion reaction in the sun where neutrinos are produced in the pp chain. On the other hand the neutrinos of focus in this paper are high-energy neutrinos that are likely produced in the same sources as the UHECRs.

3.3.1 Production and Energy loss

The production sites of high-energy neutrinos is not clear, but they are thought to be produced in the same sources as UHECRs and in this section, I will go through the most probable way of producing high-energy neutrinos in sources such as AGN.

Hadronic processes:

Hadronic processes can release neutrinos with sufficiently high energy to explain the observations here on Earth. Processes such as nuclear interactions are limited by the binding energy of the nucleus and accelerating a neutrino after its production is difficult. Therefore, a common way of producing the observed neutrinos is through the decay of pions. The most important decay is the decay of charged pions into muons and muon neutrinos as seen in equation 18

$$\pi^+ \rightarrow \mu^+ + \nu_\mu \rightarrow e^+ + \nu_e + \nu_\mu + \bar{\nu}_\mu \quad (18)$$

I will discuss two possible ways of producing these pions in two different environments.

In a proton-rich environment where the protons can accelerate up to high energies, one can produce pions through the following process

$$p + p \rightarrow \begin{cases} \pi^+ + n + p \\ \pi^- + \pi^+ + p + p \\ \pi^0 + p + p \end{cases} \quad (19)$$

The energy of these protons above a few GeV is enough to introduce the delta-baryon resonance, but usually one does not have a proton rich environment. Therefore, the most efficient way of producing pions is through the already seen delta resonance when a proton interacts with a photon, this is seen in equation 15. This process being the cooling process of UHECRs is interesting and indicates that a source that produces high energy neutrinos likely is inhabited by very energetic charged particles.

After having produced the neutrinos it also becomes important to understand their behavior during their travel to Earth. Here I will highlight two points

Neutrino oscillations: In the previous paragraph, I discussed the production of these neutrinos, but not their initial flavor. The pion decay model is known to produce a flavor composition of $\nu_e : \nu_\mu : \nu_\tau = 1 : 2 : 0$. A naive thought would be an identical composition observed on Earth, but sadly this is not the case. The reason for this is that the neutrinos' mass state can oscillate between the different flavors. Therefore, the neutrinos produced in the source will oscillate during their travel to Earth and when they reach us one would expect a uniform mix of the three flavors, $\nu_e : \nu_\mu : \nu_\tau = 1 : 1 : 1$.

Energy loss: To model the travel of a neutrino of any flavor one only needs to take into account the interaction of the neutrino with the expanding universe. Since it is so weakly interacting the only source of energy loss the flux of neutrinos will experience is the redshift created by the expansion of the Universe. This redshift is the same as the one discussed in the previous section and the neutrinos behave the same way light does in this manner with a drop in energy proportional to $(1 + z)$.

3.3.2 Detection

Neutrinos are weakly interacting matter particles and therefore are very difficult to detect. This makes them excellent candidates for the study of the Universe since they can travel large distances without interacting, but make them quite difficult to detect with high accuracy. The most famous detector and the one used in this paper is the IceCube neutrino observatory. This detector is precisely what it sounds. It is a large block of ice with a size equal to a cubic kilometer located at the South Pole. The observatory uses the ice located deep in the South Pole as a giant Cherenkov detector. The ice is instrumented with photomultiplier tubes that can detect the Cherenkov radiation produced by neutrinos interacting with the ice. More precisely the observatory is fitted with 5160 photomultiplier tubes located at a depth of 1450-2450 m. The photomultipliers are divided into 86 strings of 60 modules each. The detector is also complemented by the DeepCore detector

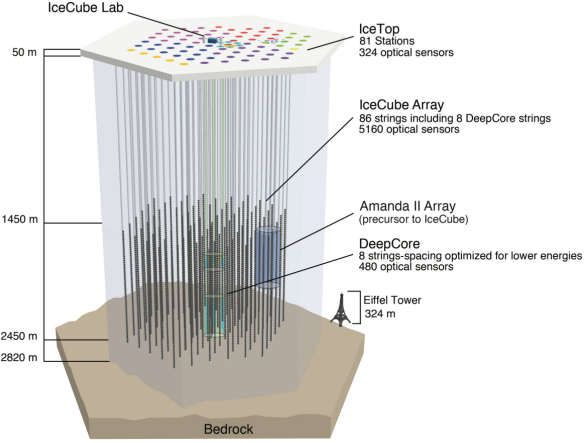


Figure 4: The IceCube neutrino observatory. The detector is located at the South Pole and is a large block of ice instrumented with photomultiplier tubes. Image taken from Andeen and Plum 2019

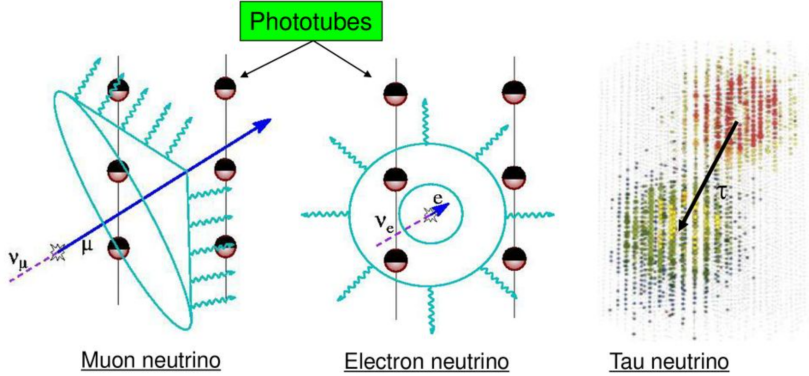


Figure 5: The difference between track and cascade events in the IceCube detector. The left image shows a track event where a muon has traveled through the detector. The middle image shows a cascade event where a neutrino has interacted with the ice and produced a shower of particles. The right image shows a double bang event where a tau neutrino has produced a tau lepton which has then decayed. Image taken from Fox 2008

which is a denser array of photomultiplier tubes located in the center of the detector. See Figure 4 for a visual representation of the detector. The energy range for this detector is from 10 GeV to 10 EeV. The interaction of neutrinos with the water molecules in the ice can produce charged leptons (muons, electrons or taus). These charged particles if energetic enough will then produce Cherenkov radiation which can be detected by the photomultiplier tubes.

The detection of neutrinos in IceCube are separated into categories which often relates to the flavour of neutrino being detected. In figure 5 one can see the distinct signature left by different flavour neutrinos. The different signatures mean that for estimating arrival direction only track events can be used, which is caused by mostly muon neutrinos. Track events have the disadvantage of being worse for estimating the energy of the neutrino, due to part of the interaction happening outside the detector. On the other hand cascade and double bang events are better for estimating the energy of the neutrino, but are worse for estimating the direction of the neutrino.

Φ_0	E_0	γ
$6.7 \times 10^{-18} GeV^{-1} cm^{-2} s^{-1} sr^{-1}$	$100 TeV$	2.37

Table 2: The model parameters for the astrophysical flux of neutrinos as measured by the Ice Cube observatory.

3.3.3 Emissivity estimates

Armed with the required knowledge above one can also make simple arguments for the sources of these neutrinos based on the observed flux here on Earth. The flux used in this paper is the diffuse flux of neutrinos as measured by the Ice Cube observatory. The flux is shown in figure 6. For any calculations, we use the astrophysical flux as modeled as a power law. The power law is of the form

$$\Phi(E) = \Phi_0 \left(\frac{E}{E_0} \right)^{-\gamma} \quad (20)$$

with Φ_0 being the normalization constant, E_0 being the reference energy and γ being the spectral index. The model parameters are seen in table 2 and taken from Abbasi et al. 2022.

The emissivity of neutrinos is calculated in the same way as for UHECRs. The only difference is the loss time. Neutrinos do not lose energy in the same way as UHECRs and therefore the loss distance will be the size of the Universe. The modeled emissivity is then approximately $1.54 \times 10^{44} \text{erg/Mpc}^3/\text{yr}$.

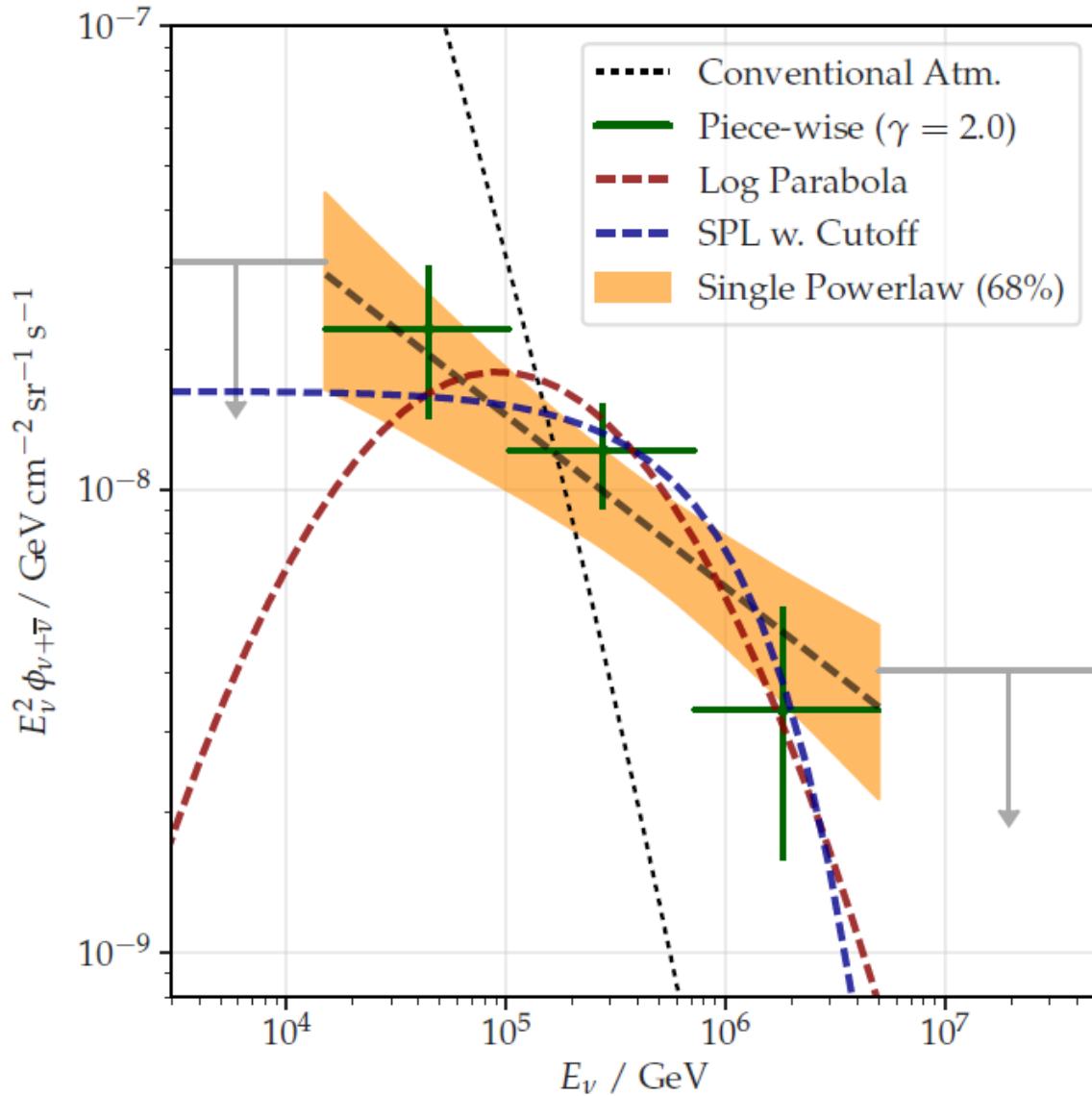


Figure 6: The diffuse flux of neutrinos as measured by the Ice Cube observatory. The y-axis on the left image is the number of events per bin. The flux is separated into contributions from atmospheric neutrinos and astrophysical neutrinos. The right image is the model astrophysical flux as measured by ICE CUBE. Images taken from Abbasi et al. 2022

4 Probing extra galactic sources

In this section one will outline some different methods and observables used to probe extra galactic sources as potential candidates for the origin of the UHECRs and/or neutrinos. The goal is to constrain our list of candidates by applying known effects and theoretical models to observed data, and to discuss the implications of these constraints. In brief, one will be discussing the energy budget of our sources, the anisotropy of the UHECRs and neutrinos, and a comprehensive time-scale analysis of the sources. In order to do so several key pieces of information is required, which will be discussed in the following sections.

4.1 Density and anisotropy

Due to the non-observation of any dipole moment in the distribution of extra-galactic UHECRs, and neutrinos as discussed in section 3 one can put strict limits on the density of sources. In collaboration 2013 they quote a density larger than $(0.06 - 5)10^{-4}\text{Mpc}^{-3}$ at a 95% confidence level. This density although not exceedingly large would still damper the idea of singular but powerful sources.

To calculate the density of sources in the Universe there are several methods. The most common method is to use the luminosity function of the sources in question. The luminosity function is a function that describes the number of sources per unit volume and luminosity. Typically, the focus is on the differential luminosity function, which is defined as

$$\frac{d\Psi(L, z)}{dL} = \frac{d^2N(L, V_c(z))}{dLdV_c(z)}. \quad (21)$$

One also can change the differential of the comoving volume into a term only depending on the redshift assuming the source population is isotropic and by multiplying with the differential comoving volume element. This transformation goes as follows,

$$\frac{d^2N(L, V_c(z))}{dLdV_c(z)} \frac{dV_c(z)}{dz} = \frac{N(L, z)}{dLdz}. \quad (22)$$

To effectively determine the LF, it's typical to divided it into two distinct components: a local term and a time evolution term. This approach involves taking the local luminosity function, calculated at a redshift $z = 0$, and then scaling it with a function that accounts for the change in redshift. The exact form of the total LF varies based on the source object, but it generally falls into two categories derived from the method of incorporating the growth term into the local LF. These methods are selected based on which best represents the observed evolution.

The two distinctions are the Pure Density Evolution (PDE) and the Pure Luminosity Evolution (PLE). The PDE model modifies the local density function to reflect changes over time, while the PLE model adjusts the local luminosity. The evolution is better represented by their equations and is given as

$$\frac{d\Psi(L, z)}{d(L)} = \begin{cases} \frac{\frac{d\Psi(L/e(z), z=0)}{d(L)}}{\frac{d\Psi(L, z=0)}{d(L)}} & (\text{PLE}) \\ \frac{\frac{d\Psi(L, z=0)}{d(L)}}{e(z)} & (\text{PDE}) \end{cases} . \quad (23)$$

For some sources which lack observational data it can be difficult to estimate a full luminosity function. Due to the lack of observation or a big bias in the catalogue selection difference sources are not constrained enough and therefore one must rely on simpler estimates to get the order of magnitude. One such method given that the lifetime of a sources is known is via simple probability. One wished to estimate their required density to produce the observed amount of sources, or in the worst case one source given its average lifetime.

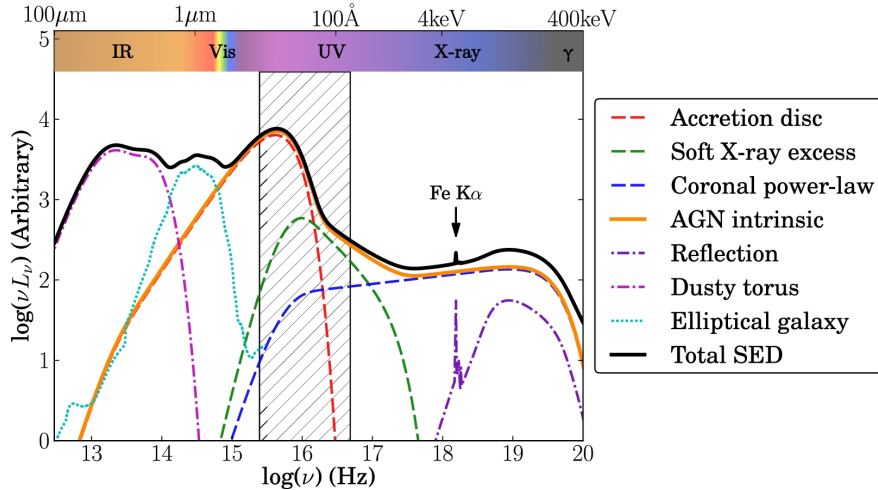


Figure 7: The spectral energy distribution of a typical AGN viewed without interference from the jet. The different components of the AGN are visible in the plot. Image taken from Collinson et al. 2016

This will in most cases serve as a lower limit, and give us a starting point for further analysis.

in order to do so, one defines the probability of seeing a single source that has a lifetime t_l up to a horizon t as

$$p = \frac{t_l}{t}. \quad (24)$$

The horizon is the redshift at which one stops finding appreciable number of your source. The required density such that one observes 1 source at present time can then be estimated as

$$n = \frac{1}{pV} \quad (25)$$

The calculation is crude, but very solid, and allows us to make lower limit estimates on sources where the Luminosity function is not defined.

4.2 SED broad band analysis

The spectral shape of emitting galaxies and galaxy cores tell us a lot about the underlying dynamics, and with this information one can start to peel away the complex layers. The spectral energy distribution (SED) of a source is a plot of the energy emitted by the source as a function of frequency. In figure 7 one can see the typical SED of an AGN in which the jet components, that is to say the synchrotron and inverse Compton components, are not dominant. The different components of the AGN are visible in the plot, and understanding how different components are created and contributing to the nearby environment will give us a better understanding of what observables one might expect from sources such as these. The main idea of these areas being good probes for UHECRs and Neutrinos is that the relativistic electrons are thought to be accompanied by relativistic protons. The true composition of the relevant areas are not known and still is a big question in this realm of research.

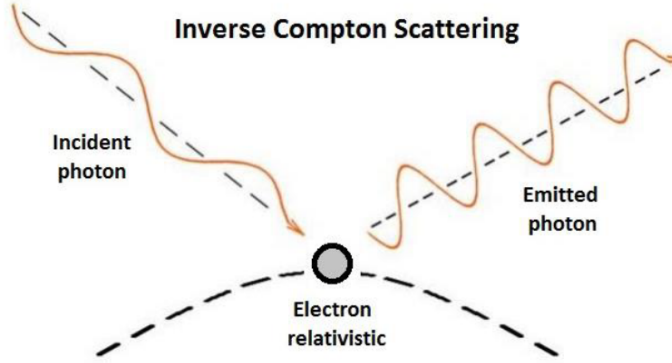


Figure 8: The inverse Compton scattering process. The process is the scattering of a low energy photon by a relativistic electron. The scattered photon will have a higher energy than the original photon. Image taken from Bennun 2020

4.2.1 X-ray energy budget

The X-ray energy budget of especially Active galactic nuclei is often used as a probe for UHECRs and neutrino emissivity. This makes the X-ray Luminosity of AGN an interesting parameter that warrant further analysis. In this sense the X-ray luminosity is often used a proxy for the total energy budget of escaping particles, but a true relation between the two is not known. The X-ray luminosity of an AGN usually has two sources of emission, the corona, and IC scattering of the synchrotron radiation in the jets. In both cases the main mechanism is thought to be Inverse Compton scattering and for that one requires relativistic electrons. Requiring relativistic electrons is a good indicator that there might be relativistic protons present as well, and following that logic one can start to estimate the energy budget of the protons.

4.2.2 Radio luminosity

4.2.3 Photon fields around AGN

In order to determine the photon fields we follow Ghisellini and Tavecchio 2009 which describe the photon fields surrounding a Blazar. The photon fields separates into different contribution from the different regions of a classic AGN as discussed in section ... The different regions are the accretion disk, the broad line region, the torus and the x-ray corona.

Accretion disk: The photon field emerging from an accretion disk if calculated by assuming a black body spectrum at each ring of an Shakura-Sunyaev disk and summing up its contributions. The temperature of each ring in the disk is given by

$$T(R) = \left(\frac{3R_S L_d}{16\pi R^3 \eta \sigma_{SB}} \left(1 - \left(\frac{3R_S}{R} \right)^{\frac{1}{2}} \right) \right)^{\frac{1}{4}} \quad (26)$$

Each ring of the accretion disk is assumed to be at the same temperature and emitting as a black-body spectrum. By using this temperature one can use the black body spectrum of an object with temperature T to find the intensity:

$$I(\nu) = \frac{2h\nu^3}{c^2} \left(\frac{1}{\exp\left(\frac{h\nu}{k_B T}\right) - 1} \right) \quad (27)$$

By integrating the intensity over all annuli of the disk one can find the total flux of the disk and from there the total energy density of the disk per frequency. This then needs to be scaled to incorporate the location of our emitting region which sits at a distance R from the accretion disk.

The resulting spectral energy density is then given by

$$U_d(\nu) = \frac{2\pi}{c} \int_{\mu_d}^1 I(\nu) d\mu \quad (28)$$

where μ_d is the cosine of the angle between the location on the disk and the normal of the disk with respect to the observer.

X-ray corona: The photon field from the x-ray corona is assumed to be a power law spectrum with a cut off at high energies. Its total energy emitted is related to the disk Luminosity by the equation $L_{cor} = fL_d$ where f is the fraction of the disk luminosity that is emitted by the corona. The spectral energy density of the corona is then given by

$$U_{cor}(\nu) = D(R) \left(\frac{\nu}{\nu_0} \right)^{-\alpha} \exp\left(-\frac{\nu}{\nu_{cut}}\right) \quad (29)$$

The factor $D(R)$ is a scaling factor that incorporates the position of the observer in similar fashion to the disk. The integral of the spectral energy density over all frequencies should equate to the total energy density in x-ray at the location of the emitting region.

The energy density of x-ray around the central engine is given by a

$$UX(R) = \frac{f_X L_d \Gamma^2}{\pi(R_X)^2 c} \left(1 - \mu_X - \beta(1 - \mu_X^2) + \frac{\beta^2(1 - \mu_X^3)}{3} \right) \quad (30)$$

where

$$\mu_X = \left(1 + \frac{R_X^2}{R^2} \right)^{-0.5}.$$

Here f_X is the fraction of the disk luminosity that is emitted by the x-ray corona, L_d is the disk luminosity, Γ is the lorentz factor of the jet, R_X is the size of the x-ray corona, c is the speed of light, β is the velocity of the observer in units of the speed of light. In short the x-ray energy density stays constant until the observer is further away where it will decrease as $1/R^2$ which is to be expected.

Broad line region: The broad band field is assumed to be emitting a black body spectrum as in 27 which peaks at the Lyman-alpha line. The Lyman-alpha line is a spectral line of hydrogen when the atomic electron transitions from the $n = 2$ to the $n = 1$ orbital corresponding to a frequency of $\nu_\alpha = 2.47 \times 10^{15}$ Hz. Similarly to the x-ray corona the spectral energy density is scaled to the region of interest and the total energy density is given by:

$$\text{UBLR}(R) = \begin{cases} \frac{f_{\text{BLR}} L_d \Gamma^2}{\pi R_{\text{BLR}}^2 c} & \text{if } R \leq R_{\text{BLR}}, \\ \frac{f_{\text{BLR}} L_d \Gamma^2}{\pi R_{\text{BLR}}^2 c \beta^3} [2(1 - \beta \mu_{\text{IR1}})^3 - (1 - \beta \mu_{\text{IR2}})^3 - (1 - \beta)^3] & \text{if } R \geq 3R_{\text{BLR}}, \\ aR^b & \text{otherwise,} \end{cases} \quad (31)$$

where

$$\mu_{\text{IR1}} = \left(1 + \frac{R_{\text{BLR}}^2}{R^2}\right)^{-0.5},$$

$$\mu_{\text{IR2}} = \left(1 - \frac{R_{\text{BLR}}^2}{R^2}\right)^{-0.5},$$

Torus: There is also assumed to be a dusty torus around the AGN emitting in infrared. The spectral energy density of the torus is also given by a black body spectrum with the temperature of the torus being set at $T_{\text{IR}} = 370$ K. The total energy density of the torus has the same relations as equation 31 but with the relevant parameters for the torus.

$$\text{UIR}(R) = \begin{cases} \frac{f_{\text{IR}} L_d \Gamma^2}{R_{\text{IR}}^2 c} & \text{if } R \leq R_{\text{IR}}, \end{cases} \quad (32)$$

For illustrative purposes one can see the total spectral energy density in figure ??.

4.3 Magnetic field constraints

4.3.1 Equipartition

The most well known estimate for magnetic field strength in astrophysical sources is through the equipartition argument. The fact that one observes synchrotron radiation implies that a source of relativistic electrons which have an energy density U_e and that these electrons are in a magnetic field with an energy density U_B . The question that one aims to answer with the equipartition argument is what is the minimum total energy in both relativistic particles and magnetic fields required to produce the observed synchrotron radiation of a given frequency. The total energy in relativistic particles and magnetic fields of a volume V is given as

$$U_{\text{tot}} = U_e + U_B = V(u_p + u_{\text{mag}}) \quad (33)$$

Here u_p is the energy density of all relativistic particles, i.e. electrons, protons and heavier ions ($Z > 1$). Ions emit very little synchrotron radiation for a given energy E compared to electrons, so little is known about their energy density, therefore it is common to assume

$$u_p = \eta u_e \quad (34)$$

where η is a constant > 1 and u_e is the energy density of the relativistic electrons. In order to estimate the energy density of the electrons one assumes their distribution as a power law $n(E) \propto E^{-\delta}$, and their energy density becomes

$$u_e = K \int_{E_{min}}^{E_{max}} E^{1-\delta} dE \quad (35)$$

In order to move one it is require to know the spectrum of synchrtron radiation for one electron in a particular magnetic field. The derivation is a tedious process, and one will give the results obtained in Wilson, Rohlfs, and Hüttemeister 2013 chapter 10.10 and 10.8. The radiated power of an electron peaks strongly around the critical frequency ν_c and one can then write a relation between a frequency ν and energy E as

$$\nu = \frac{3}{2} \frac{eB}{m_e^3 c^5} E^2. \quad (36)$$

This allows for the particle energy density to be written as

$$u_p = K \frac{\eta}{1 - 2n} \left(\frac{e}{m^3 c^5} \right)^{n-1/2} \left(\nu_{max}^{1/2-n} - \nu_{min}^{1/2-n} \right) B^{n-1/2} = KGB^{n-1/2} \quad (37)$$

by introducing the constant $n = \frac{1}{2}(\delta - 1)$.

The energy density of the magnetic field is given as

$$u_{mag} = \frac{B^2}{8\pi} \quad (38)$$

To move further one wished to eliminate the factor K from our equations, and relate it to observed properties. Wilson, Rohlfs, and Hüttemeister 2013 gives the emissivity of a synchrotron source for tangled magnetic fields as

$$\epsilon(\nu) = b(n)K \frac{e^3}{mc^2} \left[\frac{3e}{4\pi m^3 c^5} \right]^n B^{n+1} \nu^{-n} = HKB^{n+1} \nu^{-n}, \quad (39)$$

where $b(n)$ is a function of the spectral index n . The observed flux density of a source with volume V and at distance R is given as

$$S(\nu) = \frac{V}{R^2} \epsilon(\nu) \propto B^{n+1} \nu^{-n} \quad (40)$$

Using this relation one can then write the total energy density while inserting 40 as K in 37 as

$$U_{tot} = \frac{G}{H} R^2 (S_\nu \nu^n) B^{-3/2} + \frac{VB^2}{8\pi} \quad (41)$$

Given that one has measurments on distance, volume, flux density one can then estimate the magnetic field strength. One then argues that U_{tot} should have a minimum value and one then finds the magnetic field to be

$$B_{eq} = \left(\frac{6\pi G}{H} \frac{R^2}{V} S_\nu \nu^n \right)^{2/7} \quad (42)$$

This relationship between U_B and U_e at this minimum is very near the equipartition value, which is why

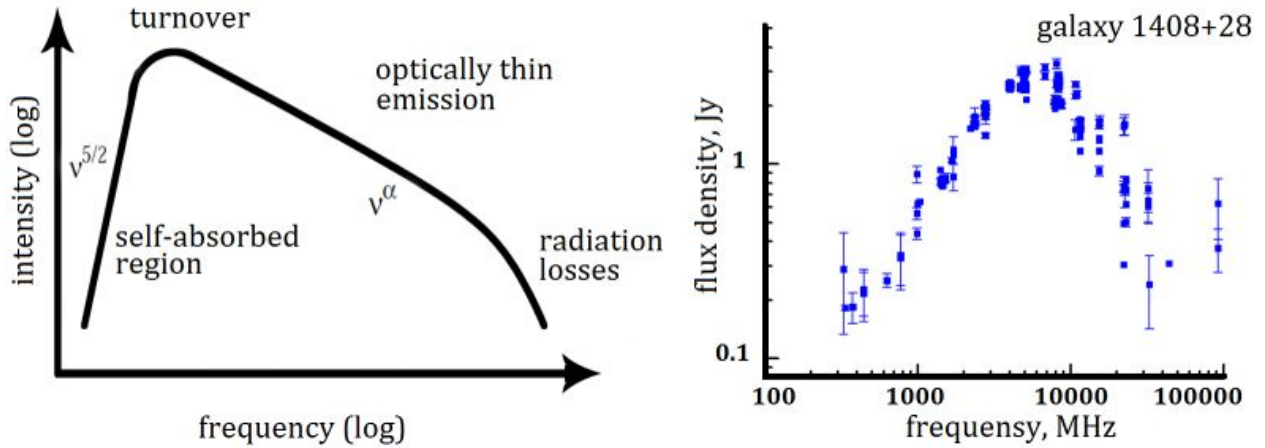


Figure 9: The synchrotron spectrum of a Giga hertz peaked galaxy. Later on one will realise that GHP galaxies and CSO occupy that same niche. Image taken from Group of Active Galactic Nuclei investigation at <https://www.sao.ru/hq/giag/gps-en.html>

this method is often called as such.

4.3.2 Self synchrotron absorption

The theory of synchrotron self absorption is a tool used previously for estimating magnetic field strength in spherically symmetric synchrotron sources. Synchrotron radiation is the product of charged particles traveling in a magnetic field. The radiation is emitted when the particles are accelerated which happens when an electron is spiraling in an uniform magnetic field. The light is usually highly polarized and is dependent on the electron energy and the magnetic field strength. Moving further along, synchrotron self absorption is the process where the synchrotron radiation is absorbed by the same electrons that produced it, and the effect of this is that any given volume of emitting plasma that radiate synchrotron radiation will have a frequency below which the radiation is absorbed. This frequency is called the turnover frequency, and one aims to show how one can estimate the magnetic field strength in the emitting plasma based on this information. The concept was first introduced by Marscher 1983, but this section relies heavily on Hirotani 2005 for the derivation.

Before we begin the derivation it is fitting to understand the spectrum of synchrotron radiation from a plasma. The spectrum is characterized by the peak frequency, also called the turnover frequency ν_m , the peak flux density S_m , and naturally the spectral index α . One referse the reader to image 9 for a simple view of the synchrotron speaktrum in question.

In order to estimate the magnetic field strenght we must assume that it is uniform and that the electron density is also uniform. From here the transfer equation for synchrotron radiation gives in Hirotani 2005

$$I_\nu = A(\alpha)\nu^{5/2}[1 - \exp(-\alpha_\nu^*x_0^*)] \quad (43)$$

where

$$A(\alpha) = \frac{3^{-\alpha}}{2} \frac{e}{c} \frac{a(\alpha)}{C(\alpha)} \left(\frac{e}{2\pi m_e c} \right)^{-3/2} B^{-1/2} \quad (44)$$

and x_0^* give the thickness of the emitting plasma along the observers line of sight. The coefficients $a(\alpha)$ and $C(\alpha)$ are tabulated values that depend on the spectral index α not to be confused with the absorption coefficient α_ν and any value denoted with an asterix is in the comoving frame.

Imagining an observer at a distance D with angle θ from the blob of plasma(as seen in figure 10), one can define the fractional thickness, which is a Lorentz-invariant quantity, as

$$\frac{x_0^*}{2R^*} = \cos(\theta + \xi) = \sqrt{1 - \left[\frac{\sin(\theta)}{\sin(\theta_d/2)} \right]^2} \quad (45)$$

Determining that $\tau(0) \equiv \alpha^* 2R^*$ is the optical depth for $\theta = 0$ one can then get the full specific intensity as

$$I_\nu(\theta) = \left(\frac{\delta}{1+z} \right) A(\alpha) \nu^{\frac{5}{2}} \left(1 - \exp \left(-\tau(0) \sqrt{1 - \left[\frac{\sin(\theta)}{\sin(\theta_d/2)} \right]^2} \right) \right) \quad (46)$$

The shape of the blob is assumed to be spherical and we can now integrate the specific intensity over the entire blob to get the total flux density as

$$S_\nu = 2\pi \int_0^{\theta_d/2} I_\nu(\theta) \cos(\theta) \sin(\theta) d\theta = \pi \sin^2(\frac{\theta_d}{2}) (\frac{\delta}{1+z})^{1/2} A \nu^{5/2} \int_0^1 [1 - \exp(-\tau(0) \sqrt{1-x^2})] dx \quad (47)$$

where $x \equiv \left[\frac{\sin(\theta)}{\sin(\theta_d/2)} \right]^2$. Here we insert what we know about the synchrotron spectrum and the turnover frequency ν_m . We derivate the flux density with respect to frequency and set it equal to zero to find the equation that realtes $\tau_\nu(0)$ and α at the turnover frequency. In order to do this one needs to know the relation between the absorption coefficient and frequency. This is given also in Hirotani 2005 as

$$\alpha_\nu^* = C(\alpha) r_0^2 k_e^* \frac{\nu_0}{\nu^*} \left(\frac{\nu_B}{\nu^*} \right)^{(-2\alpha+3)/3} \quad (48)$$

where, $\nu_0 \equiv c/r_0$ is the electron frequency, $r_0 \equiv e^2/(m_e c^2)$ and $\nu_B \equiv eB/(2\pi m_e c)$ is the cyclotron frequency.

Having the solution for $\tau_\nu(0)$ as a function of α one denotes the solution at the turnover frequency as $\tau_m(0)$. This is a tabulated value and the table from Hirotani 2005 is found in the appendix.

Using this solution one can inversly solve equation 47 for the magnetic field strength B and obtain with the small angle approximation

$$B = 10^{-5} b(\alpha) \left(\frac{S_m}{\text{Jy}} \right)^{-2} \left(\frac{\nu_m}{\text{GHz}} \right)^5 \left(\frac{\theta_d}{\text{mas}} \right)^4 \left(\frac{\delta}{1+z} \right) \text{G} \quad (49)$$

where $b(\alpha)$ is a tabulated value as well but arrises from

$$b(\alpha) = 3.98 \times 10^3 \left(\frac{3}{2} \right)^{-2\alpha} \left[\frac{a(\alpha)}{C(\alpha)} \right]^2 \left[\int_0^1 [1 - \exp(-\tau(0) \sqrt{1-x^2})] dx \right]^2 \quad (50)$$

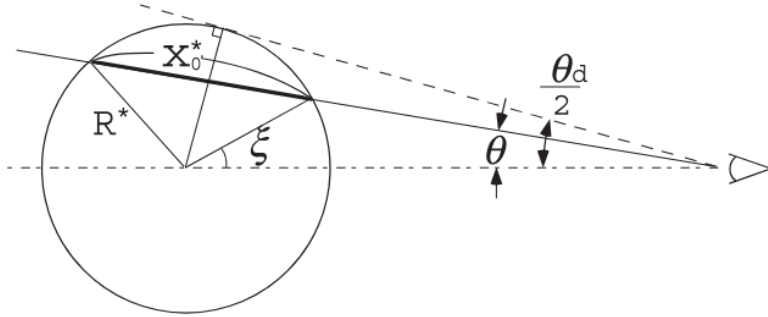


Figure 10: Schematic view of the radiative transfer in a spherical ball of plasma. Image taken from Hirotani 2005

4.3.3 Deviation from SSA and Equipartition

If one calculates the magnetic field using both SSA and Equipartition one expects to not get the exact same results, but given a big discrepancy one cannot assume all the fault lies in only the measurements. In Orienti and Dallacasa 2013 who used SSA and equipartition calculations for a small sample of CSOs, they also found a discrepancy between the two methods. The SSA had a significantly higher value for the magnetic field. This they argue can, and the weight is on can here be induced by a free free absorption effect in the source. Free free absorption is the absorption of radiation by an electron who is in close proximity to an ion. The absorption is a result of the electron being accelerated by the ion and the radiation emitted by the electron is absorbed by the ion. The effect of free-free absorption would shift the spectral peak in SSA to higher frequency and thus give a higher magnetic field strength in our calculations. This would be a good indicator that the source is harbouring ions, which one needs for UHECRs acceleration.

4.4 Time-scales analysis

In order to probe what type of sources could be responsible for the observed UHECRs and neutrinos one can use the relevant time-scales a measure. The timescales of a source will act as an indicator of the dominant processes in the source, and give us an upper boundary for what we could expect of escaping particles. The dominante timescales of a source will be source specific, so further on we will be looking at the timescales of a typical compact AGN. The relevent timescales then are the acceleration timescale, the synchrotron cooling timescale, the dynamical timescale, and the photo-pion cooling timescale.

Acceleration timescale: One starts by determining the acceleration timescale of a proton undergoing first order fermi acceleration, the acceleraiton mechanisms explained in section The acceleration timescale is given by the equation

$$t_{acc} = \frac{\eta\epsilon}{ZeBc} \quad (51)$$

Where η is the efficiency of the acceleration process with the most efficient acceleration harbouring the value $\eta \approx (1 - 10)$, ϵ is the energy of the particle, Z is the charge of the particle, e is the elementary charge, B is the magnetic field strength and c is the speed of light. Usually the value of η is taken to be 1, which is the most efficient acceleration process.

Size estimation/ dynamical timescale:

The dynamical timescale is a limit on the sources size and can be estimated several ways. The sources size is important since in order to accelerate particles the source must also be able to contain particles. If one does not have good measurments on the source size, but have good fluence measurments of an attributing

light curve one can estimate the size of the source via the variability. From the variability timescale t_{var} one can estimate the size of the source as

$$R = \frac{c\Gamma t_{var}}{1+z} \quad (52)$$

Another way of estimating the sources size is through telescope measurements. For radio sources one can achieve sufficient accuracy in measurements to estimate the size of the source. If radio if one has the full width at half maximum of the source one can relate this to the total angular size of a spherical source according to Marscher 1983 as $\theta = \theta_{FWHM} 1.8$. If one then knows the distance to the source one can get the physical/linear size of the source as

$$D_{\text{size}} = (\theta_{FWHM} 1.8) \cdot D_A(z) \quad (53)$$

Where $D_A(z)$ is the angular diameter distance to the source at its redshift z .

A third method of estimating the radius of our lobes is outlined in Wójtowicz et al. 2020. They use a relation between the total linear size of an object and the estimated relations between the semi-major axis and the semi-minor axis. The argument is that some AGN which are important for this report have relatively large aspect ratios between their axes, with an estimation equaling $b/a \approx 0.25$. From this, they introduce the effective radius of the radio lobes via

$$R_{\text{lobe}} = \sqrt[3]{ab^2 \frac{3}{4}} \approx 0.18 \times LS = 0.18 \times 2 \times a \quad (54)$$

Cooling timescales:

In the source of AGN there will be an environment of magnetic fields and photon fields that will interact with the particles. An important timescale to consider given this environment is often the synchrotron cooling timescale. This is the timescale for a particle to lose energy due to synchrotron radiation. One will have both synchrotron losses for proton and for electrons, but since one is concerned about UHECRs one will focus on protons. The synchrotron cooling timescale for protons is given by the equation

$$t_{\text{sync}} = \frac{6\pi m_p^4 c^3}{\sigma_T m_e^2 B^2 E}. \quad (55)$$

Here, m_p is the proton mass, m_e is the electron mass, σ_T is the Thompson cross-section, B is the magnetic field strength, E is the energy of the particle and c is the speed of light.

The last timescale used in this analysis is the pion production timescale. Due to the photon fields a proton will inhabit while accelerating, one needs to consider the pion production timescale. This is the timescale for a proton to interact with a photon and produce a pion. The equation is given by

$$t_{pr}^{-1}(\varepsilon_p) = \frac{c}{2\gamma_p^2} \int_{\varepsilon_{th}}^{\infty} d\varepsilon \sigma_{pr}(\varepsilon) k_p(\varepsilon) \int_{\varepsilon/2\gamma_p}^{\infty} d\varepsilon' \varepsilon'^{-2} \frac{dn}{d\varepsilon'} \quad (56)$$

where ε_p is the energy of the proton, γ_p is the Lorentz factor of the proton, ε_{th} is the threshold energy for the interaction, σ_{pr} is the cross-section for the interaction, k_p is the photon field, and $dn/d\varepsilon$ is the differential photon density.

In our analysis one will follow C. D. Dermer and Menon 2009 to set up the pion resonance timescale. σ_{pr} ,

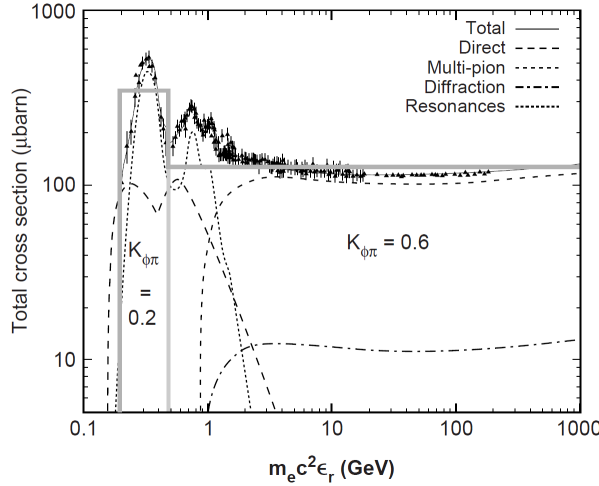


Figure 11: Pion resonance cross section, and the inelasticity of the interaction. Image taken from C. D. Dermer and Menon 2009

or the cross-section for the interaction is given by a two step function, and is given as

$$\sigma(E) = \begin{cases} 340\mu b, \text{cm}^{-2} & \text{if } 390m_ec^2 < E < 980m_ec^2 \\ 120\mu b \text{cm}^{-2} & \text{if } E > 980m_ec^2 \end{cases} \quad (57)$$

additionally the inelasticity of the interaction, or how much energy is lost per interaction, is given as

$$K(E) = \begin{cases} 0.2 & \text{if } 390m_ec^2 < E < 980m_ec^2 \\ 0.6 & \text{if } E > 980m_ec^2 \end{cases} \quad (58)$$

A Schematic view of the pion resonance cross-section and the inelasticity of the interaction is shown in figure 11.

The last important parameter in the pion production timescale is the photon field, and one will be using a photon field as described in section 4.2.3. The specific photon fields will be determined by what source one is looking at and will be clarified in due time.

5 Active Galactic Nuclei

1

1. Introduction to AGN
2. Why AGN serves as good candidates for UHECRs and neutrinos
3. The structure of AGNs
 - (a) The central engine
 - (b) The accretion disk
 - (c) The corona
 - (d) The torus
 - (e) The broad-line region
 - (f) The narrow-line region
 - (g) The jet
 - (h) The host galaxy
 - (i) Types of outflows and particle leakadge
4. The different types of AGN
 - (a) More boradly on the different types of AGN
 - (b) Compact symmetric objects
 - (c) Seyfert galaxies
 - (d) Blazar types

Active Galactic Nuclei (AGN) are an interesting topic in astrophysical studies, and since their discovery, there has been rapid advancement in understanding these phenomena. Today, AGN are known to be among the brightest entities in the night sky, but they only gained significant attention in the early 1950s. This shift occurred with the arrival of new radio observations, which revealed a new type of quasi-stellar object through the discovery of the Quasars.

Initially, these luminous objects, characterized by broad, unidentifiable spectral lines, were enigmatic to scientists. However, with the identification of more sources and their optical parts, it became clear that these were not stars but a distinct class of celestial objects. Furthermore, research done by M. Schmidt on one of the emission lines from Quasar 3C 273 opened the interpretation of these celestial objects. He found that the emission lines of quasars were similar to hydrogen, but were redshifted by a factor of 0.158, an exceptionally high value at the time according to Shields 1999. Observations at the same time also revealed significant variability in quasar luminosity, suggesting that these objects were no larger than one light year across. These observations lead to the speculation of super luminous objects located very far away from Earth. The problem was that such objects had no reasonable explanation at the time.

Observation of the surrounding galaxy of AGN with matching redshift and observation of gravitational lensing cemented the distances of these objects. In addition, the modern view of black holes which had only been a theory in the 1950s came to fruition and the idea of accretion allowed for the modern model of an AGN to be born. This modern perspective views AGN as supermassive black holes that accrete matter from surrounding gas. In addition to this the modern view of AGN also include jets, torus, and different emitting regions that are used to classify AGN.

In the most recent times, a landmark achievement was achieved in March 2021, when scientists associated with the Event Horizon Telescope project presented the first image of the supermassive black hole at the

center of the Messier 87 galaxy, located 55 million light-years away. This image, showing a bright ring surrounding a dark central region, aligns with predictions for an accreting supermassive black hole, increasing our confidence in the modern model. In addition, the 2020 Nobel Prize in physics was awarded to Roger Penrose, Reinhard Genzel, and Andrea Ghez for their work on black holes, further cementing the importance of these objects in modern astrophysics.

5.1 AGN structure and classification

The modern view of AGN is a unified model that combines the different categories of powerful luminous objects cataloged in the mid to late 20th century. These distinctions that astronomers made still have value, but to understand an AGN it is important to get a picture of the unified structure.

An active galactic nucleus is defined as a galaxy center containing a massive accreting black hole. This mass according to Netzer 2015 is defined as $M_{BH} > 10^5 M_\odot$. AGN also have an Eddington ratio exceeding the limit of $L_{AGN}/L_{Edd} = 10^{-5}$, where L_{AGN} is the bolometric luminosity, and L_{Edd} is the Eddington luminosity for a solar composition gas. These definitions help constrain what galaxies might contain an AGN, where it excludes the Milky Way by these criteria, but it fails to capture the full structure definition of an AGN. Therefore, the structure of most AGN will include several of the following components, first summarized then expanded upon:

- A close rotational dominated accretion disc around the SMBH.
- High-density gas clouds that are said to be dust-free moving at high velocities close to the black hole, in the so-called broad line region(BLR)
- Low-density gas clouds that move at lower velocities further away from the black hole in the so-called narrow line region(NLR)
- A structure of dust that is responsible for the obscuration of the central region of the AGN. This is called the torus due to its theorized shape. It lies at a luminosity-dependent distance from the SMBH, but according to Netzer 2015 this is around 0.1 - 10 pc depending on the luminosity.
- A corona of hot electrons that is thought to be responsible for the X-ray emission seen in AGN. This is thought to be located above the accretion disk.
- A relativistic jet that is thought to be powered by the accretion disk. This is not always present but is a common feature of AGN.

The reader is directed to figure 12 for a visual representation of the different components.

5.1.1 Accretion disk

An accretion disk is a natural consequence of the conservation of angular momentum. In the case of infalling matter coming close to a supermassive black hole, the matter could have some angular momentum. With this the gas should orbit the black hole at some stable distance but, due to radiative processes, fluid viscosity, and gravitational turbulence, the matter will lose angular momentum and spiral inwards. The inward spiral will eventually allow the matter to fall into the black hole. This process of inspiral is what is called accretion and the forces acting on the matter to cause the inspiral will also in the same process heat it up to high energies causing it to radiate. The radiation is closely linked to the infalling matter that is accreted onto the black hole and one can express the total luminosity of the accretion disk as

$$L_{acc} = \eta \dot{M} c^2. \quad (59)$$

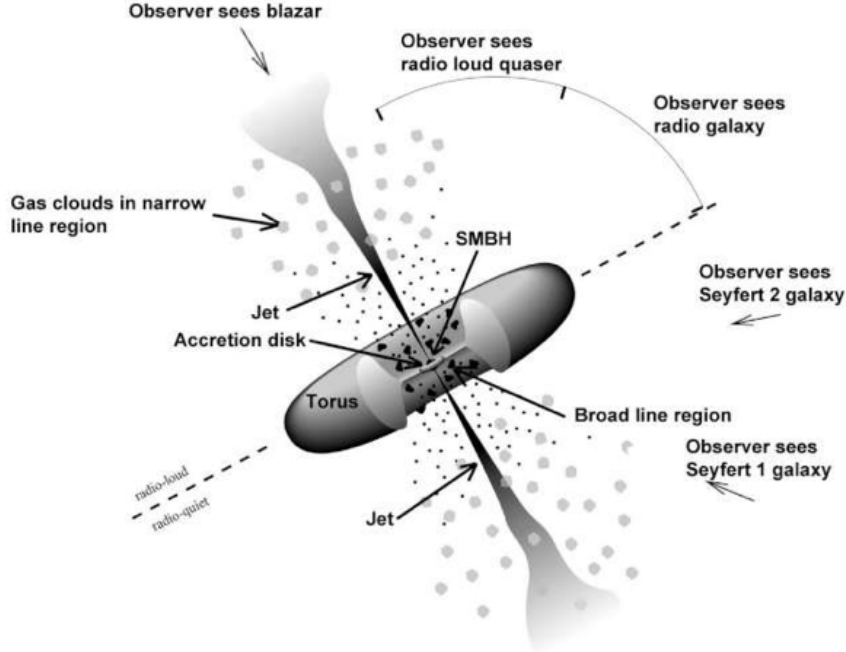


Figure 12: AGN unification

Here η is the efficiency of the accretion process, \dot{M} is the mass accretion rate and c is the speed of light.

The efficiency of the accretion disk is a function of the spin of the black hole and the radius of the innermost stable circular orbit (ISCO). The ISCO is a counter-intuitive term in classical mechanics but in general relativity the maximum speed of a particle in addition to an energy term when calculating the orbit set bounds for how close a particle can be to a black hole without spiraling in.

The accretion disk also has a bound for its maximum luminosity. As calculated for stars the Eddington luminosity sets a maximum strength for the radiation pressure of the accretion disk. This is given as

$$L_{Edd} = \frac{4\pi GMm_p c}{\sigma_T} \quad (60)$$

The heating of the accretion disc will lead to thermal radiation from the disc and this radiation will be proportional to the temperature of the disc. This temperature is radially dependent and if one assumes an optically thick but geometrically thin disk also called a Shakura-Sunyaev disk one can express the radiative surface energy flux taken from C. D. Dermer and Menon 2009(p. 106) as

$$\frac{dE}{dAdt} = F_{rad}(r) = \frac{3GM\dot{M}}{8\pi r^3} \left(1 - \beta \sqrt{\frac{r_{\text{ISCO}}}{r}} \right) \quad (61)$$

Here β is a constant that relates the fraction of angular momentum captured by the black hole, and r_{ISCO} is the radius of the innermost stable circular orbit. The temperature of the disk lie between $10^5 - 10^2$ K with emission in the optical, UV to soft X-ray range according to Abramowicz and Straub 2023.

5.1.2 Corona and X-ray emission

From highly varying X-ray observations of AGN, it became indicative that there was a source of X-rays located close to the black hole. The most contemporary idea is that a corona of energetic particles is located above the accretion disk, and through inverse Compton scattering of the optical/UV photons that arise from the accretion disk produce the seen x-ray emission.

Inverse Compton scattering is the process of a photon gaining energy from a nearby relativistic particle. Due to the increase in efficiency of up scattering a photon with an electron compared to a proton, the corona x-ray emission is thought to be dominated by electrons. The process is as follows

$$e^- + \gamma \rightarrow e^- + \gamma \quad (62)$$

5.1.3 Broad and narrow line region

Broad emission lines in the case of AGN are formed from the high-density gas clouds located close to the central black hole. The high-density parameter is inferred from the fact that one only sees broad emission from permitted line transitions (e.g. hydrogen Lyman and Balmer, iron, and magnesium). High densities allow for collisional de-excitation and in doing so prohibit so-called forbidden transitions. The broadening is an indication that these gas clouds are moving at huge velocities around the massive objects. This implies that they are located close to the black hole and receive the name the broad line region

Narrow emission lines are on the other hand formed in low-density gas clouds. The low densities are inferred from the fact that one sees both permitted and forbidden line transitions. They are narrow lines due to their velocities being substantially lower than the innermost gas clouds, and from here are thought to be located further away from the black hole, in the narrow line region.

5.1.4 Dust torus

The dust torus is a structure of dust that is thought to be located quite close to the black hole (0.1 - 10 pc). The main argument for the existence of this structure is the obscuration of the central region of the AGN. This obscuration is part of the unification scheme of AGN and was backed by the detection of polarized broad lines in AGN with their central core obscured. This polarization is what we would expect if some dust was obscuring the central region since the only light one sees is the light that is scattered into the line of sight according to Mason 2015. Further, the same study on the dust torus have also says that the torus is not uniform but clumpy and quite dynamic with both in and outflows of matter depending on the state of the central engine.

5.1.5 Jets

A jet is a highly collimated outflow of plasma. The origin of the plasma is thought to be the accretion disk and the hot corona above it. These regions that have a high density of charged particles will under the influence of a magnetic field be accelerated and collimated into a jet-like structure. The energy mechanism which powers the jet is not fully understood, but the most prevalent theory is the Blandford-Znajek process. It says that the rotation of the accretion disk induces a magnetic field that will interact with a rotating black hole, effectively extracting energy from the black hole and supplying it to the jet. The jet structure extends far beyond the local area of the AGN maintaining a stable configuration over these distances. The classification of these jets is usually divided into two groups according to Walg et al. 2013, FRI and FRII. They are differentiated by their luminosity where FRI jets are less luminous and have a more diffuse structure

while FRII jets are more luminous and have a more stable structure reaching further out. To add to this distinction it is thought that FRII jets are a product of an efficient accretion disk while FRI jets are a product of an inefficient accretion disk. This is discussed in Bian and Zhao 2003 where they show that radio quiet and Seyfert 1 galaxies have lower accretion efficiency while radio loud galaxies have higher accretion efficiency. Beyond the energy and their structure, the jets are also notable for their emission of non-thermal radiation such as synchrotron and inverse Compton radiation.

5.2 Types of AGN

Before the unification of the AGN astronomers named the puzzling objects based on their observational properties. These names are still used to this day and are useful since their observational properties are important parameters for further study. The different classifications are important in understanding which objects could have the potential to produce the different observables one looks for in the night sky. Therefore, it seems appropriate to discuss some different types of AGN and their observational properties. The classification in this section is heavily based on Sanders 2021.

Type I and II AGN: One distinguishes type I and type II AGN based on the presence of broad emission lines. In other words, this distinction is a matter of a visible nucleus or not. Type I refers to sources whose nucleus is exposed to the observer and whose spectrum has both narrow and broad emission lines. Type II refers to sources whose nucleus is obscured by a torus and therefore mainly has narrow emission lines.

Blazars: The most extreme class of AGN. These sources are distinguished by their relativistic jets that are pointed towards the observer. This jet produces both synchrotron and Inverse Compton gamma rays and are extremely variable over short timescales. The emission is also highly polarized. Often and including in this report one divides Blazars into subgroups based on the emission lines. The two most common are BL Lacs and Flat spectrum radio quasars (FSRQs). The difference between the two is the presence of broad emission lines, where BL Lacs have no broad emission lines while FSRQs do. In addition, the distinction comes from the type of jet structure thought to be associated with the source. FRI jets for BL Lacs and FRII for FSRQs.

Radio galaxies: Jetted AGN that as the name suggests are very bright in the radio band. They usually refer to AGN viewed edge-on, where the torus might block the emissions from the accretion disk. The orientation of Radio galaxies gives way to strong synchrotron radiation, and they are often used to study the jet structure of AGN.

Seyfert galaxies: Spiral galaxies that have a bright nucleus. They are bright in the optical band and have a smaller active region than radio galaxies. They are often divided into two groups Seyfert I and Seyfert II where the distinction comes from type I and II. The galaxies also show quite high variability indicating a small emitting region.

Compton thin AGN: A way of distinguishing AGN that can be quite useful. These AGN have lower absorption compared to Compton-thick AGN, which allow more X-rays to escape making them easier to identify.

All these different distinctions are a help in understanding what processes one might be observing. The different dominant bands indicate different processes being in the line of sight, and by considering the modern structure of AGN one can then try to determine the underlying dynamics.

6 Compact symmetric objects

1. Introduction to CSOs
2. What is a CSO
3. more on the structure of CSOs
4. The different types of CSOs
5. The prevalence of CSOs
6. CSO as candidates for UHECRs and neutrinos
 - (a) Hillas criterion, Flux of X-ray compared to diffuse flux of UHECRs and neutrinos
 - (b) Kinetic jet power
 - (c) Timescale analysis

Introduction to CSOs

Compact Symmetric Objects have seen a revival the last year with the publication of Kiehlmann, Lister, et al. 2023 and Readhead et al. 2023. The original discovery of CSOs was in the 1980s when according to Kiehlmann, Lister, et al. 2023 Phillips and Mutel discovered a class of compact extragalactic radio galaxies with symmetric radio structures, or harbouring a compact double radio source which was not the core. This was a break from the usual suspects of most jetted-AGN which usually shows great effect of relativistic beaming. Following the discovery of the compact double source more discoveries of CSOs were made, and in the 90s the original motivation for the CSO classification was given. According to Kiehlmann, Lister, et al. 2023 this classification lead to the misidentification of AGNs as CSO and rendering the classification less useful. In the last year the classification has been revisited and a updated list of criteria for CSOs has been given. This paper will follow the new classification of CSOs and use the updated list of CSOs from Kiehlmann, Lister, et al. 2023.

The classification of CSO can be summarized in four points taken from Kiehlmann, Lister, et al. 2023.

1. Size requirement: No projected radio structure larger than 1kpc. This has an exception to relic regions which might be signs of previous activity.
2. Symmetry requirement: Evidence of emission on both sides of the core.
3. Variability requirement: The source should not exhibit fractional variability of 20% or more per year
4. relativistic requirement: The source components should not show signs of superluminal motion greater than $v_{app} = 2.5c$

The size requirement is a key feature of CSOs since it is what makes them compact, and has previously been used to classify CSOs. Structures larger than 1kpc are often referred to as medium symmetric objects(MSO) and structures larger than that as Large symmetric object(LSO). The reason for these limits is that it approximately corresponds to the boundary between regions dominated by the black hole and the region dominated by the galaxy, and region dominated by the galaxy and the region dominated by the extra galactic environment. This then places CSOs in the region where the black hole is the dominant force. In addition to this size requirement, Kiehlmann, Lister, et al. 2023 added a caveat. Some CSOs show relic regions which are signs of previous activity. These regions can extend to larger distances than the 1kpc limit, but should not be the dominant feature of the source.

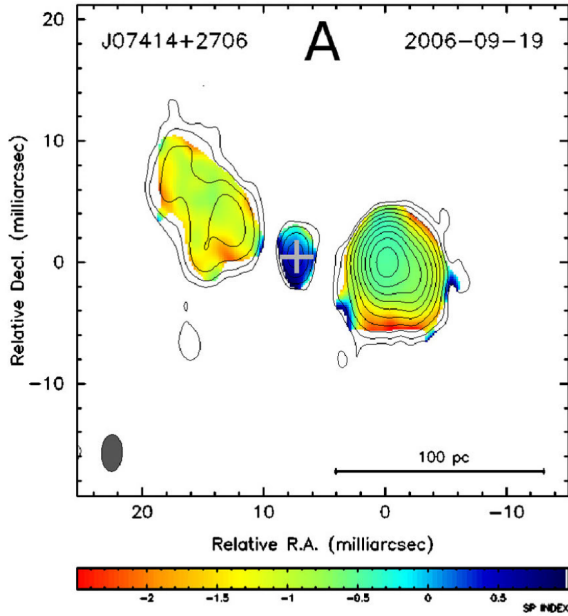


Figure 13: The radio structure of CSO J0741+2706. The core is determined from the flat spectrum component and the symmetry of the radio lobes. Image taken from Tremblay et al. 2016

The symmetry requirement also has some caveat. CSOs are objects that show any symmetric emission, but not necessarily of similar magnitude. In addition, the placement of the core is either inferred from a compact flat spectrum component, or from the symmetry of the radio lobes. In figure 13 one can see how one would determine the core placement from both the flat spectrum component and the symmetry of the radio lobes.

The last two criteria are the newest addition made by Kiehlmann, Lister, et al. 2023 and is the best way of separating CSOs from other jetted AGNs. The low variability and lack of relativistic beaming has always been a key feature of CSOs, but since they were not included in the original classification there have been misidentification. An example quoted in Kiehlmann, Lister, et al. 2023 is the source PKS 1543+005 which shows strong variability and additionally the jet is projected on both sides of the core, giving the illusion of a compact double. With these new criteria one can be more certain that the sources in the catalogue are similar enough in nature to be able to make more general statements about them.

6.1 Sub Classification of CSO

Moving further along the classification of CSOs one now realises that there are two types of CSOs. CSO 2 and CSO 1. In CSO 2 sources one consider it edge brightened where there is significant luminosity in the radio lobes compared to the core. In CSO 1 sources one consider it edge dimmed where the luminosity of the radio lobes are significantly lower than that of the core. The origin of the two types of CSOs are thought to be the same, where CSO 1s represent failed CSO 2s. One will get back to the origin later in the report.

The fact of the matter is that also the CSO 2 class can further be subdivided. This extra subdivision into CSO 2.0, 2.1, and 2.2 is on the basis of its morphology. In the number of Compact symmetric objects which succeed into becoming CSO 2s will go through different phases all with different characteristics. In figure 14 one can visualise the different phases of CSO 2 sources. The phases can analogously be compared to the different phases of shock evolution in supernovae.

CSO 2.0: According to Sullivan et al. 2024 the CSO 2.0 phase evolves analogously to FRII radio galaxies.

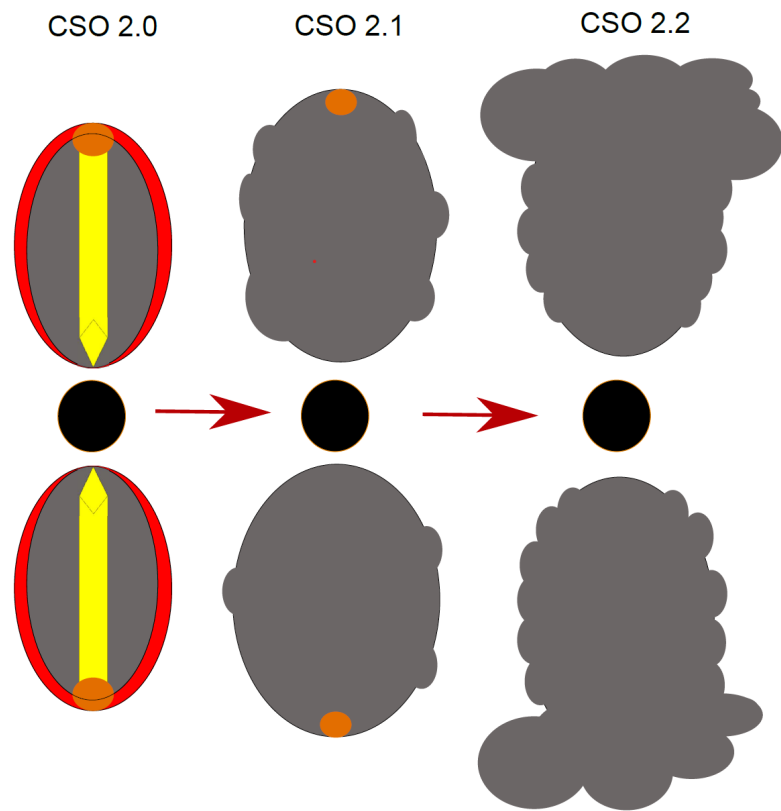


Figure 14: The different phases of CSO 2 sources. Image taken from Sullivan et al. 2024

The edge-brightened lobes which contain prominent hot spots are similar to typical features of a relativistic jet pushing into the ambient medium. As Sullivan et al. 2024 points out, classical jet models entail the jet collides with the ambient medium and forms two shock front, the forward shock and the reverse shock. From shock models the jet power L_j is what determines the velocity of the forward shock, and in Sullivan et al. 2024 the shock model used gives values similar to observation of CSO 2.0 lobe velocity ($v_c = 0.2c$) and mach number of approximately 200.

CSO 2.1: The mid life or CSO 2.1 is the transition of relativistic jet propagation into the sonic or subsonic regime. The category is often hard to define and is often contaminated by a mix of CSO 2.0 and CSO 2.2. Nevertheless, it remains a separate category since there is still power in the hotspots and the lobes continue to expand but decelerate.

CSO 2.2: The late life of CSOs or CSO 2.2 is the phase where the jet has decelerated to transonic speeds and the lobes are no longer expanding vertically as a result of jet pressure. The lobes are still expanding due to convectively rising turbulent plumes. When the plumes and the ambient densities are equal the lobes will stop expanding vertically and start expanding horizontally. Sullivan et al. 2024 compares it to the characteristic mushroom cloud of volcanic which in this author's opinion paints a very nice image.

This separation of CSOs will become important since certain environments are more favourable for the production of UHECRs and neutrinos. The most promising candidate are CSO 2.0 sources since they have the highest jet power and the highest velocity of the lobes.

6.2 Origin of CSOs/Fueling

According to Readhead et al. 2023 a possible method of fueling these objects is through tidal disruption events. Due to the short lifetime of these objects continued discrete fueling events become a good candidate for the ignition of the jets. Energetically one would assume that one needs a massive star to be able to fuel the CSO 2 jets, but it is argued in Sullivan et al. 2024 that this might not be the only solution. They argue that smaller mass stars which encounter the black hole could have sufficient magnetic flux to ignite the extraction of the black holes angular momentum. The method proposed in Blandford and Znajek 1977 relate the extraction of black hole angular momentum to the jet power via

$$L_j = \frac{1}{6\pi c} \Omega_{BH}^2 \Phi_{BH}^2 \quad (63)$$

After the TDE one expects the magnetic flux to disperse around the BH as $\Phi_{BH} \approx \Phi_* \left(\frac{R_H}{R_p} \right)^2$ where R_H is the black hole horizon and R_p is the pericenter radius of the stellar encounter. In addition, the magnetic field could be amplified via strong dipolar dynamo action or magneto-rotational instability. The magnetic field could be strong enough to match the jet powers one observes in CSOs today even though the original stellar mass was low. The caveat here is that amplification of the magnetic field is required to reach sufficient levels.

Along with the energetics one can put simple tests on this hypothesis by looking at the fallback time of debris onto a central black hole. This is also done in Sullivan et al. 2024 which quote the fallback time as

$$t_f = 0.5 \text{yr} \left(\frac{M_{BH}}{10^8 M_\odot} \right)^{1/2} \left(\frac{M_*}{M_\odot} \right)^{-1} \left(\frac{R_*}{R_\odot} \right)^{3/2} \quad (64)$$

For the TDE hypothesis to be correct one would expect the fallback time to be of the order of the lifetime of the CSO 2.0, which is $t_f \approx 1000$ years. From the equation above red giants become a good candidate as they have a large radius and a low mass, and with a SMBH of $10^8 M_\odot$ the fallback time is of the order of

1000 years.

Small sizes and finite lifetime are good indicators for transient events, and this is quoted in Sullivan et al. 2024

6.3 Catalogue of Bona fide CSO

With the new criterias for CSOs Kiehlmann, Lister, et al. 2023 begun compiling a bone fide list of Compact symmetric objects. This new catalogue will serve as the testing grounds for their ability to produce UHECRs and neutrinos. The catalogue is a list of 79 sources which are somewhat split between the four different subclasses as seen in table 4 where only the CSO with a spectroscopic redshift have been given a class. The full source catalogue is listed in table 3.

The vetting process done in Kiehlmann, Lister, et al. 2023 is thorough and the extended list of what they call A class candidate include an Additional 167 sources which have a high likelyhood of being CSOs. In additon to this they have a list of 1164 B class candidates which are sources that have a lower likelyhood of being CSOs, and therefore require a large follow up study to confirm. The vetting process rejected 1765 sources which were claimed to be CSOs or CSO candidates in other sources and catalogue created since the 1990s. This then creates a great starting block for further investigation, and with the introduction of more sources more extensive catalogues and luminosity functions can be created.

Table 3: Catalogue of bona fide CSOs. Data taken from Kiehlmann, Lister, et al. 2023

ID	R.A.	Dec.	z	Ang_size	Lin_size	ν_t	S_ν	Class
J0000+4054	00:00:53.08	+40:54:01.81	nan	124.0	nan	0.323	2.06	nan
J0003+4807	00:03:46.04	+48:07:04.14	nan	16.2	0.139	2.123	0.348	nan
J0029+3456	00:29:14.24	+34:56:32.25	0.517	29.1	0.180	0.8	2.0	2.1
J0111+3906	01:11:37.32	+39:06:28.10	0.66847	8.0	0.056	4.0	1.33	2.0
J0119+3210	01:19:35.00	+32:10:50.06	0.0602	100.0	0.115	0.4	4.0	2.2
J0131+5545	01:31:13.82	+55:45:12.98	0.003649	23.0	0.016	0.657	0.31	2.2
J0132+5620	01:32:20.45	+56:20:40.37	nan	12.2	0.104	3.42	0.6	nan
J0150+4017	01:50:19.61	+40:17:30.02	nan	103.0	0.882	0.4	2.0	nan
J0204+0903	02:04:34.76	+09:03:49.26	nan	33.0	0.282	1.3	2.0	nan
J0237+4342	02:37:01.21	+43:42:04.18	nan	120.0	nan	0.3	0.868	nan
J0402+8241	04:02:12.68	+82:41:35.13	nan	72.0	0.616	0.4	0.4	nan
J0405+3803	04:05:49.26	+38:03:32.24	0.05505	42.0	0.044	0.07	5.5	2.0
J0425-1612	04:25:53.57	-16:12:40.23	nan	99.8	0.854	0.363	1.449	nan
J0427+4133	04:27:46.05	+41:33:01.10	nan	7.0	0.060	3.3	0.74	nan
J0440+6157	04:40:46.90	+61:57:58.57	nan	30.0	0.257	1.7	0.24	nan
J0706+4647	07:06:48.07	+46:47:56.45	nan	63.0	0.539	0.777	1.81	nan
J0713+4349	07:13:38.16	+43:49:17.21	0.518	35.0	0.217	1.9	2.09	2.0
J0735-1735	07:35:45.81	-17:35:48.50	nan	28.8	0.246	1.4	3.0	nan
J0741+2706	07:41:25.73	+27:06:45.42	0.772139	26.0	0.193	1.0	1.05	2.0
J0754+5324	07:54:15.22	+53:24:56.45	nan	26.0	0.223	1.24	0.634	nan
J0825+3919	08:25:23.68	+39:19:45.76	1.21	70.7	0.591	0.517	1.77	2.1
J0832+1832	08:32:16.04	+18:32:12.12	0.154	30.7	0.081	1.5	1.2	1
J0855+5751	08:55:21.36	+57:51:44.09	0.025998	75.0	0.039	0.3	1.5	2.1
J0906+4124	09:06:52.80	+41:24:30.00	0.0273577	11.1	0.006	1.5	0.06	1
J0909+1928	09:09:37.44	+19:28:08.30	0.027843	14.7	0.008	6.0	0.12	1
J0943+1702	09:43:17.23	+17:02:18.97	1.601115	20.4	0.175	4.0	0.4	2.0
J1011+4204	10:11:54.18	+42:04:33.38	nan	115.0	0.984	0.424	1.16	nan
J1025+1022	10:25:44.20	+10:22:30.00	0.045805	19.8	0.018	1.0	0.09	1
J1035+5628	10:35:07.04	+56:28:46.79	0.46	38.0	0.221	1.3	1.87	2.0
J1042+2949	10:42:36.51	+29:49:45.15	nan	45.0	0.385	0.7	1.0	nan
J1111+1955	11:11:20.07	+19:55:36.01	0.299	15.5	0.068	1.305	1.1	2.0
J1120+1420	11:20:27.81	+14:20:54.97	0.362	101.0	0.507	0.5	3.89	2.0
J1135+4258	11:35:55.99	+42:58:44.65	nan	29.0	0.248	1.0	1.45	nan
J1148+5924	11:48:50.36	+59:24:56.36	0.01075	54.8	0.012	6.149	0.573	1
J1158+2450	11:58:25.79	+24:50:18.00	0.203	46.0	0.152	2.0	1.25	2.2
J1159+5820	11:59:48.77	+58:20:20.31	1.27997	70.2	0.591	0.6	1.9	2.0
J1204+5202	12:04:18.61	+52:02:17.62	nan	54.0	0.462	0.7	1.4	nan

ID	R.A.	Dec.	z	Ang_size	Lin_size	ν_t	S_ν	Class
J1205+2031	12:05:51.50	+20:31:19.00	0.02378857	22.0	0.010	1	0.14	2.1
J1220+2916	12:20:06.82	+29:16:50.72	0.002	46.8	0.002	0.074	0.65	1
J1227+3635	12:27:58.72	+36:35:11.82	1.975	58.8	0.499	1.2	2.14	2.0
J1234+4753	12:34:13.33	+47:53:51.24	0.373082	27.4	0.140	1.4	0.36	2.1
J1244+4048	12:44:49.19	+40:48:06.15	0.813586	70.0	0.529	0.405	2.03	2.2
J1247+6723	12:47:33.33	+67:23:16.45	0.107219	5.0	0.010	1.16	0.36	2.0
J1254+1856	12:54:33.27	+18:56:01.93	0.1145	4.14	0.008	6.0	0.13	1
J1311+1658	13:11:23.82	+16:58:44.22	0.081408	27.0	0.041	0.447	0.824	1
J1313+5458	13:13:37.85	+54:58:23.91	0.613	57.0	0.384	0.555	1.65	2.2
J1326+3154	13:26:16.51	+31:54:09.52	0.36801	68.0	0.345	0.5	7.03	2.2
J1335+5844	13:35:25.93	+58:44:00.29	nan	12.9	0.110	4.9	0.9	nan
J1347+1217	13:47:33.36	+12:17:24.24	0.121	100.0	0.215	0.4	8.86	2.2
J1400+6210	14:00:28.65	+62:10:38.59	0.431	67.6	0.378	0.5	6.56	2.2
J1407+2827	14:07:00.40	+28:27:14.69	0.077	11.0	0.016	4.9	3.0	2.1
J1413+1509	14:13:41.66	+15:09:39.51	nan	15.0	0.128	2.5	0.47	nan
J1414+4554	14:14:14.85	+45:54:48.73	0.186	30.5	0.094	0.693	0.396	2.1
J1416+3444	14:16:04.18	+34:44:24	nan	81.0	0.693	0.7	2.1	nan
J1434+4236	14:34:27.86	+42:36:20.06	0.452	68.3	0.393	0.074	1.67	2.2
J1440+6108	14:40:17.87	+61:08:42.88	0.445365	30.0	0.171	0.4	0.48	2.1
J1443+4044	14:42:59.32	+40:44:28.94	nan	123.4	nan	0.292	1.55	nan
J1508+3423	15:08:05.70	+34:23:23.00	0.045565	280.0	0.247	0.23	0.25	2.1
J1511+0518	15:11:41.27	+05:18:09.26	0.084	10.6	0.017	0.4	0.48	2.0
J1559+5924	15:59:01.70	+59:24:21.84	0.0602	11.0	0.013	0.15	0.23	1
J1602+5243	16:02:46.38	+52:43:58.40	0.105689	250.0	0.478	0.15	1.48	1
J1609+2641	16:09:13.32	+26:41:29.04	0.473	61.3	0.362	1.1	5.44	2.1
J1645+2536	16:44:59.07	+25:36:30.64	0.588	39.0	0.258	1.0	1.1	2.1
J1723-6500	17:23:41.03	-65:00:36.61	0.01443	7.0	0.002	2.7	4.48	2.1
J1734+0926	17:34:58.38	+09:26:58.26	0.735	12.8	0.093	2.3	1.22	2.0
J1735+5049	17:35:49.01	+50:49:11.57	0.835	8.0	0.061	6.4	0.972	2.0
J1816+3457	18:16:23.90	+34:57:45.75	0.245	45.5	0.174	0.44	0.983	2.1
J1826+1831	18:26:17.71	+18:31:52.89	nan	74.0	0.633	0.308	1.08	nan
J1826+2708	18:26:32.11	+27:08:07.95	nan	41.0	0.351	1.0	0.34	nan
J1915+6548	19:15:23.82	+65:48:46.39	0.486	36.0	0.216	0.5	0.83	2.1
J1928+6815	19:28:20.55	+68:14:59.27	nan	128.1	nan	0.074	1.04	nan
J1939-6342	19:39:25.02	-63:42:45.62	0.183	42.6	0.130	1.4	15.0	2.0
J1944+5448	19:44:31.51	+54:48:07.06	0.263	48.8	0.196	0.778	1.77	2.0
J1945+7055	19:45:53.52	+70:55:48.73	0.101	40.6	0.075	1.8	0.929	2.2
J2022+6136	20:22:06.68	+61:36:58.80	0.2266	29.0	0.104	4.086	2.64	2.1
J2203+1007	22:03:30.95	+10:07:42.59	1.005	11.0	0.089	4.427	0.306	2.0
J2327+0846	23:27:56.70	+08:46:44.30	0.02892	1300.0	0.744	0.09	1.0	1
J2347-1856	23:47:08.63	-18:56:18.86	nan	33.4	0.186	1.8	0.66	nan
J2355+4950	23:55:09.46	+49:50:08.34	0.23831	90	0.337	0.7	2.93	2.2

Table 4: Classification of CSOs in the catalogue.

Class	Number of sources	Percentage of total
CSO 1	11	14.0
CSO 2.0	17	21.5
CSO 2.1	15	19.0
CSO 2.2	11	14.0
No class	25	31.6

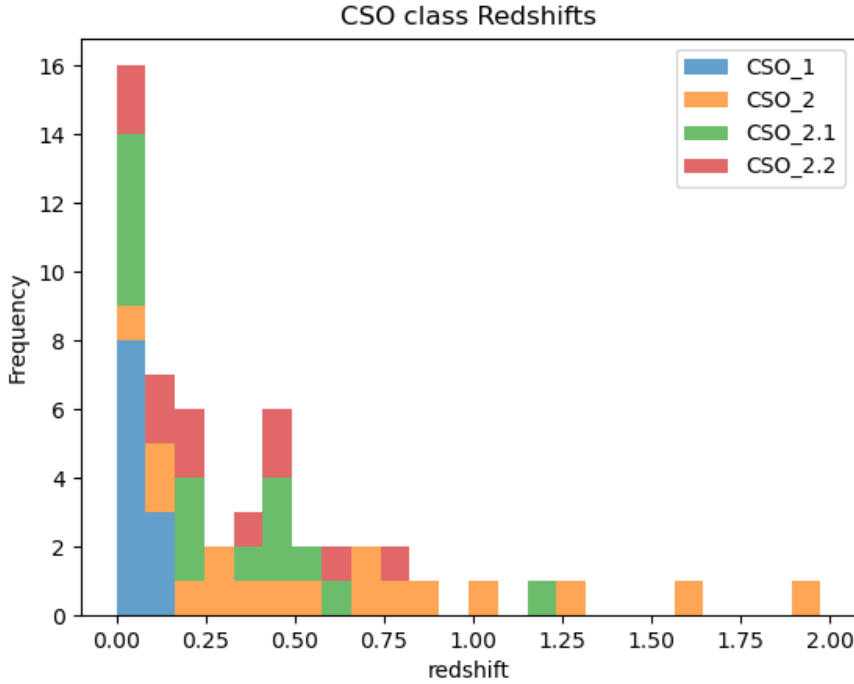


Figure 15: Distribution of redshift of different classes

As seen in Albers et al. 2024 one ...

6.4 Characteristic of CSOs

Given the new criteria and the new catalogue one can start to peel away the characteristics of CSO. The first thing one can study is the redshift distribution. In figure 15 one sees the spread of our bona fide CSOs across redshift. The immediate observation is that the majority of CSO 1 sources are in close vicinity. Additionally, the majority of CSO 2.1 and 2.2 are also in closer vicinity compared to CSO 2.0. This distribution is expected since one assumes one is observing the higher end of the luminosity function of CSOs, and therefore the most luminous sources will be the ones that are observed at higher redshifts.

One can compliment this observation in figure 17 where one sees the radio luminosity at peak frequency of CSOs as a function of redshift. Here there is a clear trend toward lower luminosity as we move to lower redshifts. This helps to confirm the observation bias of the redshift distribution. One has also put a line at $z = 0.017$ which is the redshift cutoff of $50Mpc$, the distance which is a limit for the GZK horizon.

Moving to different features of CSO it is very common to study the linear size relations of CSOs. Linear size maintain close relations with the emmission of the source, and will relate to the age of the sources, and the jet power. In figure 16 one can see the radio luminosity at peak frequency of CSOs as a function of linear size.

The figure shows a clear relation between linear size and emissivity in radio. This relation is expected since the amount of energy deposited into the lobes will affect the size of the lobes. CSO 1 occupy their own region in the plot giving foundation to the distinction between CSO 1 and CSO 2. The figure does not show a clear distinction between CSO 2.0, 2.1, and 2.2, but one can see that the most luminous sources are CSO 2.0 for a given linear size.

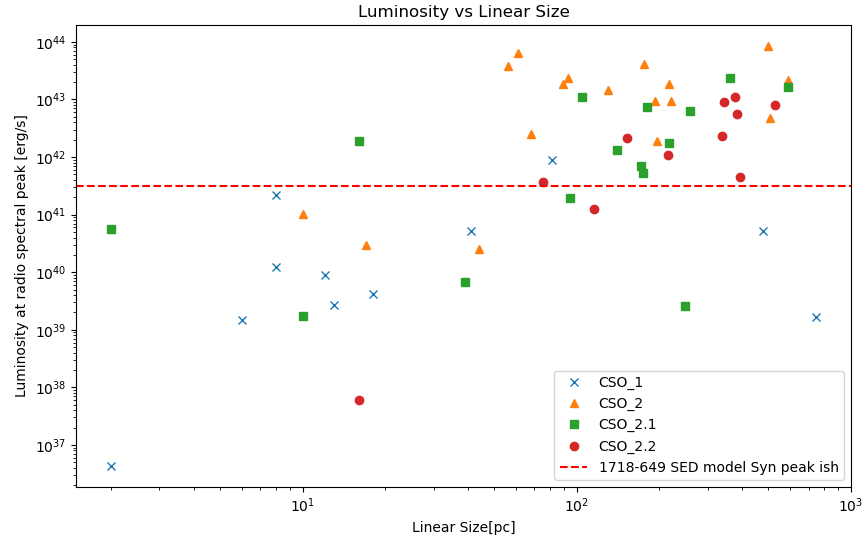


Figure 16: The radio luminosity at peak frequency of CSOs as a function of linear size.

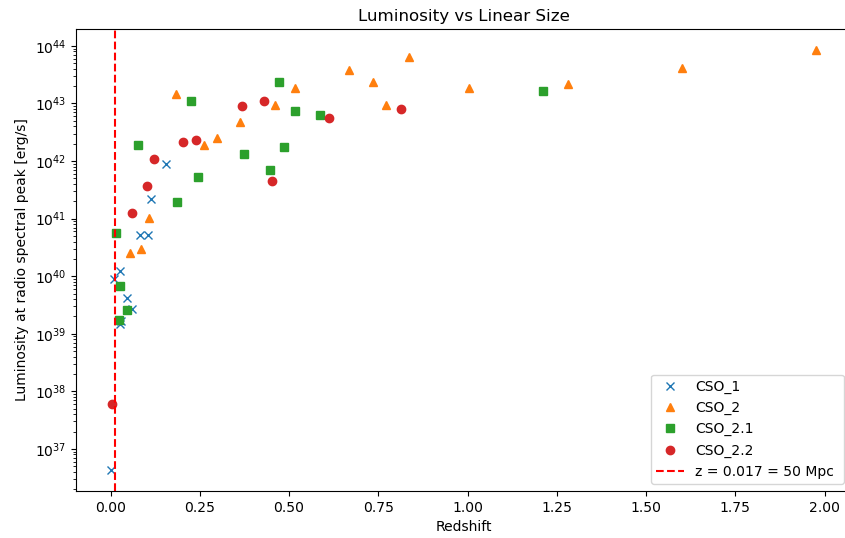


Figure 17: The radio luminosity at peak frequency of CSOs as a function of redshift.

6.5 Prevalence of CSOs

The number density of these object is of utmost importance in the search for UHECRs emitters. The author has not found a dedicated luminosity function of these sources, and due to the new criteria proposed in 2024 one would imagine previous luminosity function might be contaminated, as the previous CSO catalogues have. On the other hand one can use the lifetime of our objects and make lower limit predictions of the number density of these sources.

From section 4 one defined a method using the lifetime of our objects. The lifetime of CSOs is of the order of 5×10^3 years. One can see also that the redshift at which one find an apreciable amount of sources which is also backed in Kiehlmann, Readhead, et al. 2023 is at redshift $z = 0.9$. The required number density of these sources to view one source at present time is therefore $1.2 \times 10^4 \text{Gpc}^{-3} = 1.2 \times 10^{-5} \text{Mpc}^{-3}$. This is a lower limit since one does view more than one CSO at present time. In addition the surveys used in creating the catalogue go down to 0.7Jy at 5GHz and 1.5Jy at 2.7GHz meaning that one is only viewing the most luminous sources. If less luminous sources are also able to produce UHECRs one could expect a plethora of sources.

The number density of the order of 10^{-5}Mpc^{-3} does not meet the required density of 10^{-4}Mpc^{-3} for UHECRs, but since this is a lower limit for the high luminosity sources, one then requires a bigger part of the luminosity function to be able to produce UHECRs as well.

Name	z	Class	ν_t	S_{ν_t}	ν_{5GHz}	θ_{lobe}	$S_{\nu_{5GHz}}$
J0029+345	0.517	2.0	0.8	1.178	5	2.1	0.766
J0111+3906	0.66847	2.0	4.0	0.88189	5	0.95	0.862
J0119+3210	0.0602	2.2	0.4	0.5125	5	9.85	0.205
J0405+3803	0.055	2.0	0.07	2.554	5	2.7	0.418
J0713+4349	0.518	2.0	1.9	0.94311	5	1.45	0.722
J1035+5628	0.0460	2.0	1.3	1.0659	5	1.6	0.741
J1158+2450	0.203	2.2	2	0.588	5	4	0.566
J1347+1217	0.121	2.2	0.4	1.3947	5	1	0.488
J1407+2827	0.077	2.1	4.9	2.9375	5	1.2	2.350
J2022+6136	0.2266	2.1	4.086	1.57256	5	2	1.787
J2355+4950	0.238	2.2	0.7	1.5450	5	1.8	0.791

Table 5: Overlapping sources between the NRAO catalogue and Kiehlmann, Lister, et al. 2023 and the extracted values scaled to represent one lobe hotspot.

7 CSO as sources of UHECRs and neutrinos

7.1 Magnetic field strength

In order to estimate magnetic field strength, one outlines two methods in section 4.3.1 and 4.3.2. Now one only needs to collect data. Of the two methods, the equipartition method is the most reliable and the easiest to collect data for, but uses the assumption of equipartition, an assumption that is not necessarily the case. The SSA method is more difficult to obtain data for, due to the necessity of collecting data at the correct frequency, but does not need an assumption between the magnetic field strength and the energy density of the particles. In addition to this, both values will work as great cross-checks for different parameters in the system. For Synchrotron Self-Absorption (SSA) $B \propto R^4$, while for equipartition $B \propto R^{-2/7}$.

From table 3 one is given the turnover frequency and its corresponding flux density. The problem here is that this value is for the entire source and not any hotspot or lobe. In order to derive the appropriate value, one needs to know the size of a lobe, and importantly the fraction of emitted radiation that stems from that lobe compared to the rest of the source. This is a difficult task ridden with selection bias, but one will make an effort to estimate the magnetic field strength. In order to estimate both the SSA and equipartition magnetic fields, one will turn to a catalogue of 374 strong flat spectrum radio sources, called The VSOP 5 GHz Continuum Survey: The Pre-launch VLBA Observations, Fomalont et al. 1996. This catalogue measured high-resolution radio images of some sources contained in table 3 at 5GHz. These images will allow us to estimate the size of an individual lobe, here we chose the most powerful lobe, and the fraction of the total flux density that comes from this lobe. The same fraction will then be applied to the turnover flux density given in table 3 to estimate the turnover flux density from this lobe. Additionally, the NRAO catalogue also gives flux densities measured at 5GHz, allowing us to estimate the equipartition magnetic field strength based on an assumption of the spectral index. One finds an overlap of 10 sources between the two catalogues, and the extracted values can be found in table 5.

From here one can estimate the magnetic fields via both methods.

The result of the magnetic field estimations is a little varied, but the most reliable numbers indicate a magnetic field strength between 5×10^{-3} and 1×10^{-1} G. Here, one relies most heavily on the equipartition argument due to the SSA estimation being very biased, as the estimation of the lobe size is wrong for turnover frequencies lower than the imaging. The lobe size estimation is based on the images from the 5 GHz survey, and as one sees in figure 19, the magnetic field strength from SSA calculations is heavily dependent on the difference between the turnover frequency and the frequency of the observation. The SSA still gives values for the magnetic field strength that are in the same order of magnitude as the equipartition method at turnover frequencies closer to the measured frequency and even go above.

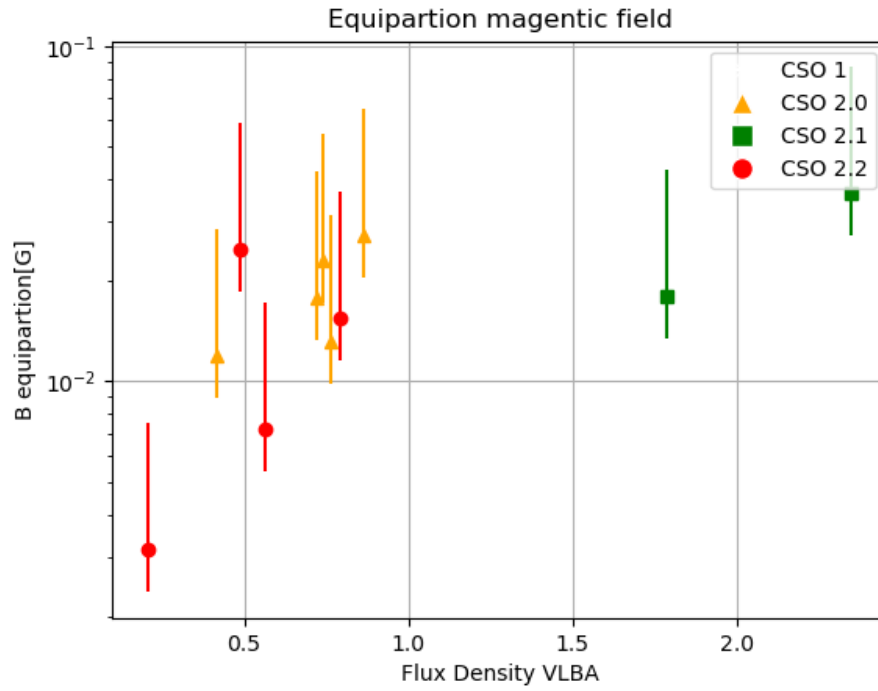


Figure 18: Magnetic field strength estimated from the equipartition method. The errorbars are calculated from the span of values obtained from different spectral index ranging from 0.6 to 1.3.

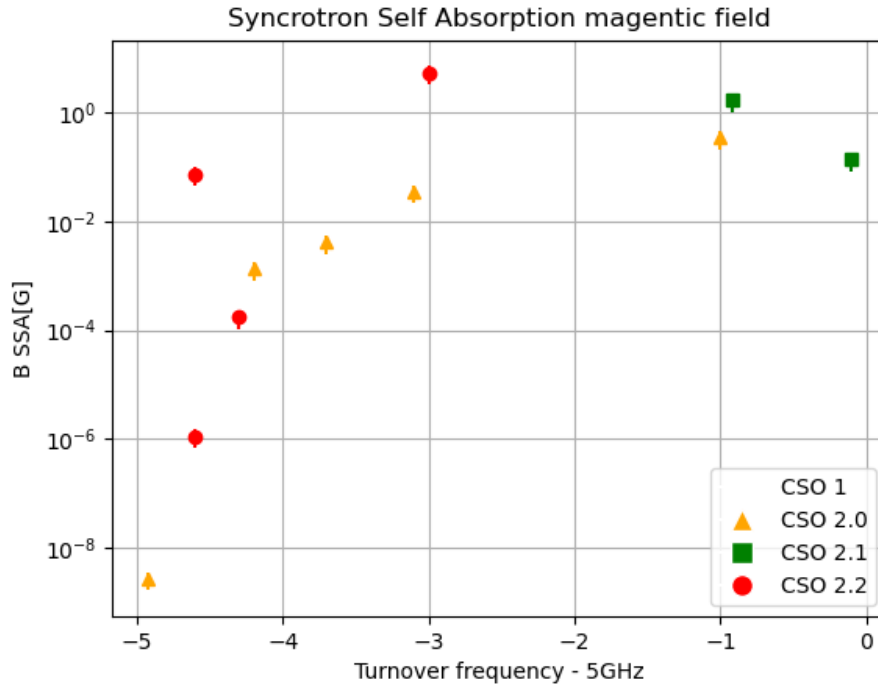


Figure 19: Magnetic field strength estimated from the SSA method. The errorbars are calculated from the span of values of $b(\alpha)$ obtained from different optical thickness. $b(\alpha)$ ranges from 1.08 to 2.38.

The equipartition calculations are also greatly affected by the choice of spectral index, as seen by the large error bars, but place the sources neatly in the same order of magnitude as the best SSA calculations. For SSA calculations that go above the equipartition values, one can have several explanations. Firstly, it could be that the equipartition argument does not hold and that the magnetic field is stronger than the equipartition value; this can be investigated by looking at jet power. Secondly, it could be that there are other factors than synchrotron self-absorption that make the source optically dense. If one includes free-free absorption, one could shift the turnover frequency to a higher value, resulting in a higher magnetic field measurement. This is not investigated in this work but is a possible explanation for the high magnetic field strength. For the continued work in this thesis, one will use the equipartition magnetic field strength as the most reliable value but will also consider the SSA magnetic field strength as a possible value. The general magnetic field of a CSO in all classes would then be $B = 10^{-2}$ G.

The estimation of the radius of our emitting regions in the previous section can be put under question. In order to estimate the precise value of our emitting regions, one would ideally measure the flux at the turnover frequency in order for the most flux not to drop under the sensitivity of the telescope. Even given this, Marscher 1983 would estimate the angular size of the source is still $\theta_{\text{true}} = 1.8 \times \theta_{\text{FWHM}}$. For some sources in table 5, one measures close to the turnover frequency, but for most, a more thorough consideration could be in order. The equipartition method is not as sensitive to the size of the source, but one should still be careful not to take the values at face value.

In order to do so, another method of estimating the radius of our lobes is outlined in Wójtowicz et al. 2020. They use a relation between the total linear size of an object and the estimated relations between the semi-major axis and the semi-minor axis. The argument is that CSOs have relatively large aspect ratios between their axes, with an estimation equaling $b/a \approx 0.25$. From this, they introduce the effective radius of the radio lobes via...

$$R_{\text{lobe}} = \sqrt[3]{ab^2} \frac{3}{4} \approx 0.18 \times LS = 0.18 \times 2 \times a \quad (65)$$

With this estimation, one can estimate the size of the lobes for the sources in table 5, and compare the resulting values to the radii obtained from the FWHM of the images in the NRAO catalogue. Here, one will note that this is an estimation of lobe size and not necessarily the hotspot which we are interested in. The results...

7.2 Energy budget

Via the energy budget of the CSOs, one can get an idea of where it is possible to accelerate protons to UHECR energies. The most natural place is in the Hillas diagram, where one can compare the size and magnetic field strength of the system to the maximum energy of the proton. From our magnetic field estimations, one can see that the magnetic field strength is between 10^{-2} and 1 G. The radius of our emitting region is on the order of 2 pc to 10 pc when the lobe expands. It would be reasonable to assume that as the lobe expands, the magnetic field strength decreases, but as it expands, more energy is also being fed into the hotspots. Therefore, one could assume a magnetic field strength of 10^{-1} G for the biggest lobes as well. The choice of magnetic field strength and radius of the emitting region can be compared to other candidates for emitters and is shown in figure 20.

7.2.1 x-ray power

From the figure, it becomes clearer that CSOs are a class worthy of being investigated further; both their lobe size and their magnetic field strength make them great candidates. As with all potential sources, one

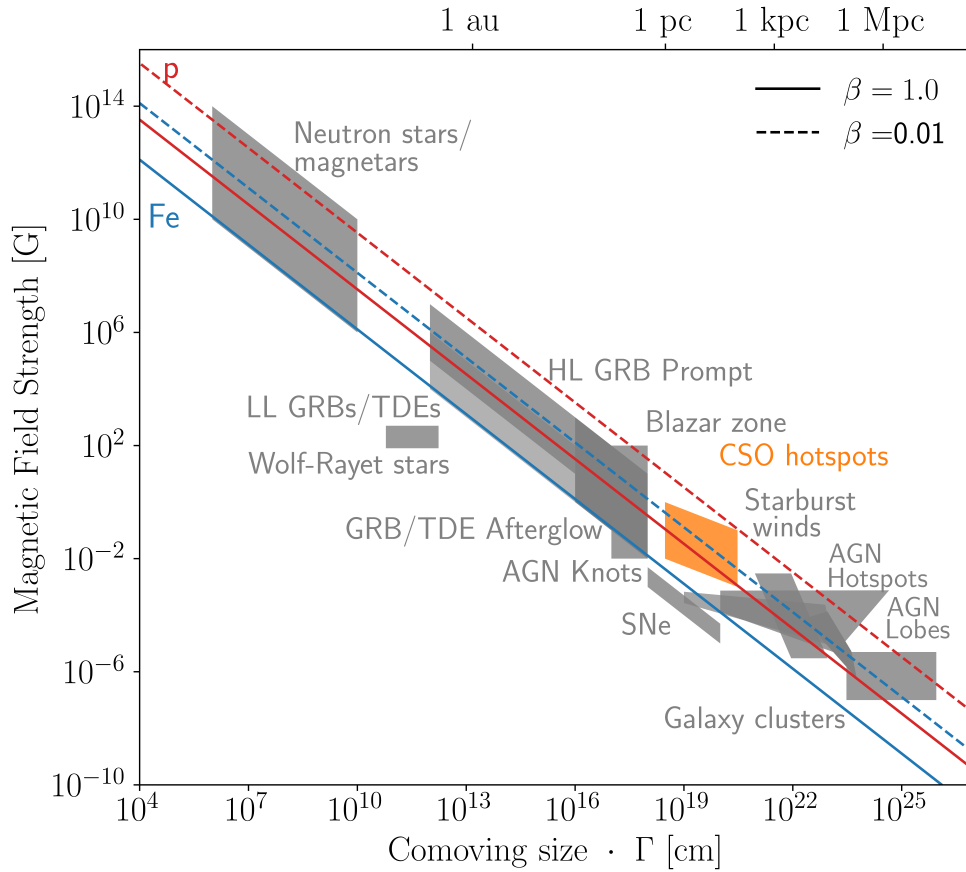


Figure 20: Hillas diagram for the CSO. The red line represents the maximum energy of the proton that can be accelerated in the system, and blue is the same just for Iron.

Name	z	Class	$L_{\text{X-ray}}$
J0111+3906	0.66847	2.0	70
J0119+3210	0.0602	2.2	<1.0
J0713+4349	0.518	2.0	394
J1511+0518	0.084	2.0	30
J1939-6342	0.183	2.0	6
J1944+5448	0.263	2.0	7.31
J1945+7055	0.101	2.2	12
J2022+6136	0.227	2.1	112
J2355+4950	0.238	2.2	13

Table 6: X-ray flux of the CSOs in table 3 found in the data set in Wójtowicz et al. 2020. The X-flux is given in units of 10^{42} erg/s.

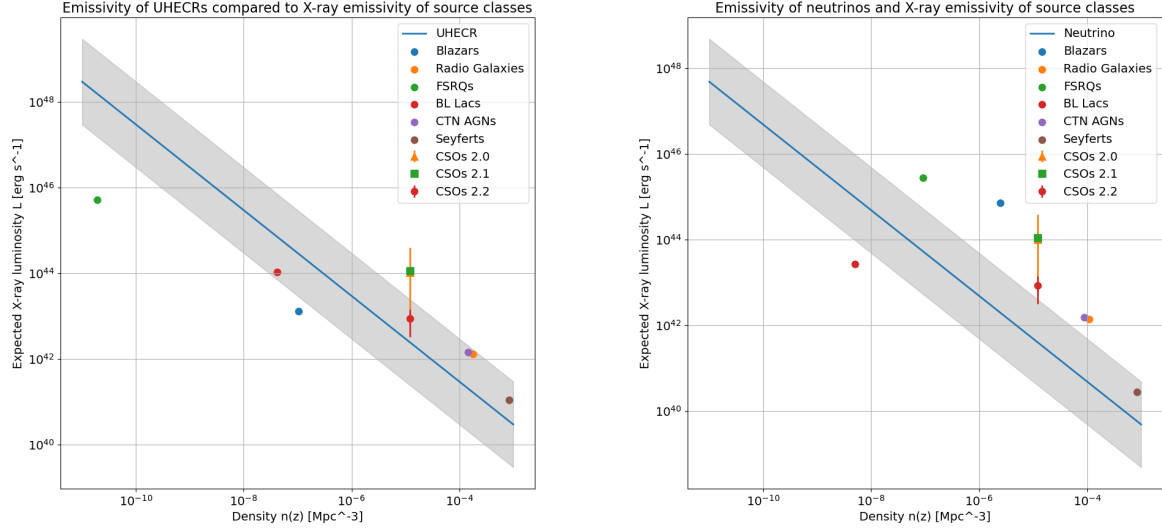
observes that a highly efficient acceleration mechanism is needed to accelerate the protons. The efficiency of acceleration is described by the β factor in figure 20. The CSO hotspots separate themselves from usual AGN hotspots, which are attributed to large lobes at the end of the jet in huge radio galaxies. The more compact hotspots in CSOs might be more efficient in accelerating protons, but this needs to be looked into further.

7.2.2 X-ray power

In studies such as Jacobsen et al. 2015 and George et al. 2008, one discusses the possibility of using the X-ray flux or hard X-ray flux as a proxy for hadronic acceleration. This is a common start in trying to probe the biggest emitters of neutrinos and UHECRs, and it is worth looking at CSOs this way as well. The biggest caveat with this method is that one usually attributes the X-ray flux to the core region, and then one might have different mechanisms for acceleration than one has in the hotspots. In the case of our model of a CSO SED, one immediately sees that the total X-ray flux from the X-ray corona will be a factor of the total accretion luminosity. For our model of timescales later in the chapter, one assumes the fraction to be $f_X = 0.3$, and for this, one received a typical total X-ray corona flux of 3×10^{42} erg/s. This number is quite a lot higher than what was found by Bronzini et al. 2024, who, using two spectral models, found an X-ray flux for two compact sources, PKS 1718-649 and TXS 1146+596, to be just shy of 10^{41} erg/s. In addition to this estimate, Wójtowicz et al. 2020 cites the X-ray flux of 17 CSOs, and here one will do another cross-correlation with the CSOs in table 3. The results can be seen in table 6.

After cross-correlation, one is left with 9 objects that are in both catalogues. The X-ray flux of these objects spans the range between $6 - 394 \times 10^{42}$ erg/s for CSO 2.0, which has the most data. CSO 2.2, with three data points, does not have any that exceed 13×10^{42} erg/s, and the lone CSO 2.1 sits at a powerful 112×10^{42} erg/s. With these values, one can compare them to other jetted AGN like BL Lacs and blazars. One will do this by looking at the total X-ray emissivity of the sources and comparing it to the local emissivity of the UHECRs. The total X-ray emissivity is given by $Q_{\text{X-ray}} = L_{\text{X-ray}} n_{\text{CSO}}$. The results can be seen in figure ??.

The amount of data collected is very low, and one cannot make any strong conclusions from this, but using the values as a benchmark, one can see that the X-ray emissivity of the CSO 2.0 and 2.1 spans a sizeable area above the local emissivity of UHECRs and neutrinos. CSO 2.2 seems to emit X-ray at a lower rate but still powerful enough to exceed the local emissivity of UHECRs. In previous work, I have found that even though the X-ray flux is a good indicator of relativistic particles, in most cases electrons, there still is work to be done relating it to UHECRs and neutrinos. Given that the X-ray flux of the CSOs surpasses the local emissivity of UHECRs and neutrinos significantly, one can say that the CSOs are also good candidates for UHECRs and neutrino production when compared to other AGN.



(a) UHECRs emissivity compared to X-ray luminosity of AGN classes

(b) Neutrinos emissivity compared to X-ray luminosity of AGN classes

7.2.3 Radio power

7.2.4 Jet power

The jet power of jetted AGN can be an important parameter in constraining parameters such as particle energy density, and as one will argue, if one can move away from equipartition. If the jet energy is carried by particles, one can relate the comoving particle density to the stationary frame jet power P_j as,

$$\frac{P_j}{2\Omega_j R^2 c \beta (\Gamma m_e c^2)} \quad (66)$$

This is for a two-sided jet, where Ω_j is the jet opening angle in sr. The jet power relation here includes the assumption that the jet is carried by electrons and that the jet power is related to the bulk Lorentz factor of the plasma outflow. By using a general particle distribution for electrons, for example, as seen in equation 72 and including a factor to account for kinetic energy being carried by protons, one can represent the jet power as a function of the kinetic energy carried by particles. One adds to this the power required to expel magnetic field-laden plasma given as

$$P_b = 2 \frac{B^2}{8\pi} \Omega_j R^2 c \beta \Gamma^2 \quad (67)$$

By now including the equipartition magnetic field B_{eq} and rewriting the kinetic terms as done in section 4.3.1, one can relate the minimum jet power as a function of the equipartition magnetic field. One is skipping a few steps of derivation, but this can be found in C. D. Dermer and Menon 2009 on page 136. The result is the minimum jet power of the system as a function of the equipartition magnetic field strength given as

$$P_j(B_{eq}) = \frac{14}{3} \pi c \beta \Gamma^2 R^2 \frac{B_{eq}^2}{8\pi} \quad (68)$$

The last quantities that need to be estimated are the bulk Lorentz factor and, importantly, jet β , or the speed of expansion into the surrounding medium. The bulk Lorentz factor of our jet is estimated to be $\Gamma < 1.1$ since CSO jets are not relativistically beamed. The last value is the expansion speed of the jet, which will vary from class to class. In the case of CSO 2.0, one will estimate a value of β between $0.1 - 0.4$ c. In Sullivan et al. 2024, they cite the expansion speed of a CSO 2.0 to be approximately $200 \times c_s = 200 \times 250$ km/s, where c_s is the sound speed. This gives a value of $\beta = 0.166$ c. Part of the definition of CSO 2.1 is that the jet is decelerating, and therefore one would expect β to lie between 0.1 and 8×10^{-4} c. Lastly, the speed of the jet in CSO 2.2 is by definition extremely low or non-existent, where the apparent motion of emitting bubbles is due to adiabatic expansion. Therefore, one argues that the speed of any emitting blob is to move at the speed of sound in the medium, and therefore $\beta = 8 \times 10^{-4}$ c. For values of jet energy derived this way, one will argue that they mostly will work for CSO 2.0 due to the fact that their jet opening angle has not evolved greatly from their initial state.

One will need to compare this jet power to another method in order to investigate the underlying dynamics. In Blandford and Znajek 1977, one finds a relation between the jet power and the accretion rate of the system. The relation is given as

$$P_j = k \dot{M} c^2 \quad (69)$$

where k is a constant that depends on the rotation velocity of the system's black hole. The various values of k range from 0.3 to 2, where $k = 2$ represents a maximally spinning black hole, $\Omega_{\max} = c^3/2GM$. One can estimate the accretion rate as a fraction of the X-ray luminosity via some simple assumptions. Like our broadband SED modeling, one assumes that the X-ray luminosity is a fraction of our accretion luminosity $L_{\text{X-ray}} = f_X L_{\text{d}}$. The accretion rate is given as $\dot{M}_{\text{d}} = \eta M c^2$ where η is the efficiency of the accretion disk. By substituting the mass accretion rate as a function of the X-ray luminosity, one can get a simple estimate for the jet power. The resulting jet power is given as

$$P_j = \frac{k}{\eta f_X} L_{\text{X-ray}} = \alpha L_{\text{X-ray}} \quad (70)$$

Here, α is a constant that absorbs the other constants since they are most likely dependent on each other. One will utilize the same table as before to estimate the jet power of the CSOs, but one needs to define the equipartition magnetic field for them as well. Since one does not have NRAO data for these sources, one will use the relation between linear size and radius to estimate the radius of the lobes. Otherwise, S_v is given in Wójtowicz et al. 2020 with the corresponding X-ray luminosity. The jet power can then be seen in figure 22.

It becomes clear that the gap between X-ray flux and CSO 2.2s is too large to account for the jet power of the system. This is not surprising since all X-ray flux measured is attributed to the core region but this will likely not be the case. As seen in the SED figure 23 the x-ray flux can have multiple sources, of which upscattering by relativistic electrons happening outside the x-ray corona is very likely. Therefore, this comparison has some big caveat when it comes to X-ray estimated jet power. On the other hand The minimum jet powers of CSO2.0 and 2.1 are more inline with the power estimated via the X-ray luminosity. This might indicate that more of the x-ray flux from these sources is related to the x-ray core, and our assumption of the x-ray flux being a proxy for jet power is more valid.

7.3 Time scales

Looking at characteristic timescales for CSOs is a powerful tool for understanding the maximum energy that can be obtained from the system. In section 4, one outlined the general method, and here one will present the results for CSO 2s.

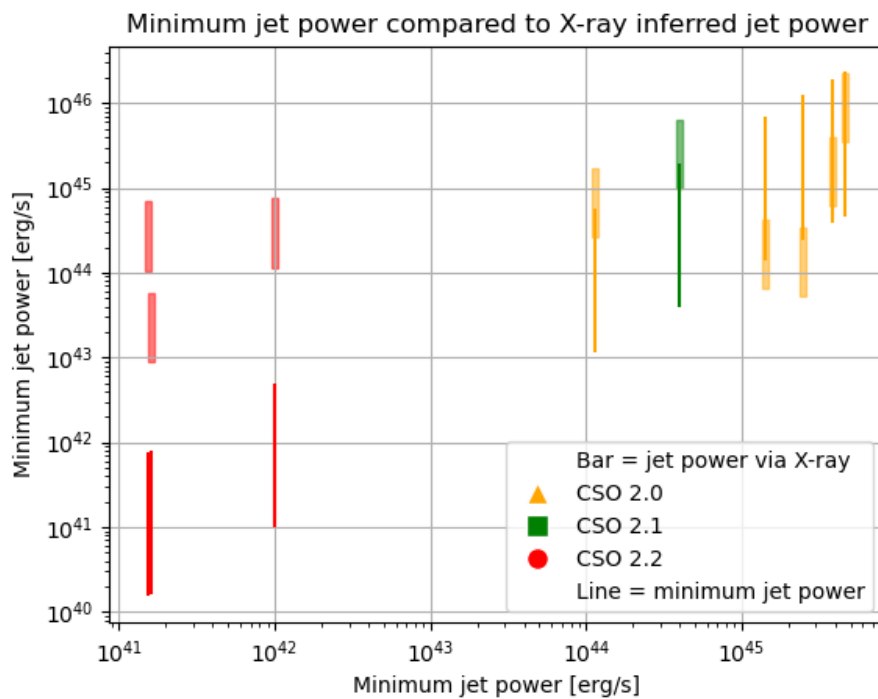


Figure 22: Jet power of the CSOs in table 3. The jet power is calculated using the minimum jet power argument based on magnetic field equipartition. The bars in line with each line represent the estimated jet power based on the X-ray luminosity varying the value of α in equation 70.

While the line representing minimum jet power is varying based on β values.

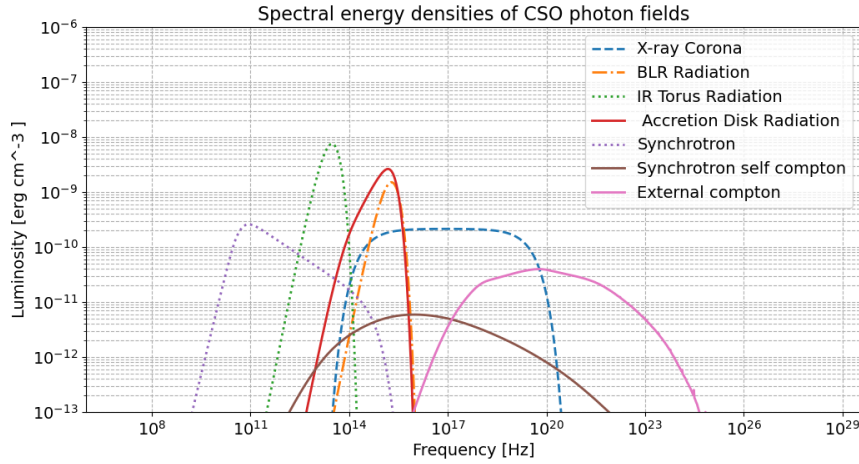


Figure 23: SED of the different regions in the CSO. The SED is based on the parameters in table 7.

With given data obtained from measurements, one will define conservative estimates for an acceleration region in the CSO. The regions of interest are the hotspots created during the CSO 2.0 and 2.1 stages, and one will observe that these are good regions for acceleration. The first constant that needs to be estimated is the size of our emitting system. From observations, it is clear that the radio lobes expand significantly during the CSO lifetime. From radio variations, which are on the order of tens of years, a reasonably conservative estimate for the size of the lobes is $R_{\text{lobe}} = 2 \text{ pc}$. In addition to this size requirement, one will also include the lifetime of the source, which is on the order of 10^3 years.

In estimating the magnetic field strength, one found the values of typical lobes to be $B = 10^{-2} \text{ G}$ from the equipartition argument. This value has been found before in previous literature and is a reasonable lower limit for the magnetic field strength. It is important to note that the magnetic field strength is a very important parameter and yet bears significant uncertainty. It may very well be that the magnetic field strength is higher than this value, and one will discuss this in the following sections.

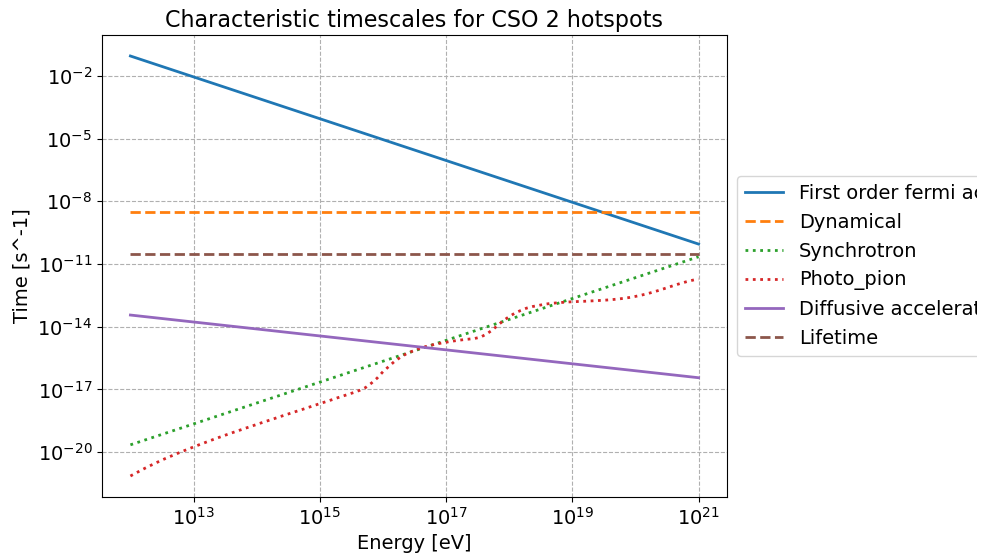
For the photopion production, one will use the photon field as described in section 4, where the used parameters can be found in table 7. This field is based on the field of a much larger AGN, but one assumes for this discussion that the field is similar in the CSO. One can compare this generated field to the ones presented in Bronzini et al. 2024, where they find a similar magnitude and shape of the resulting SED. A significant note is that the field is also not strongly beamed, giving room for other parts of AGNs to be seen. The resulting SED is seen in figure 23. The exact shape of the SED is not incredibly important for the following discussion, but the broad shape and magnitude are important. The exact shape of the SED will become more important when one starts looking for observational signatures of the acceleration, such as gamma rays, and here one can use the model SED and minimize the parameter space to find the best fit.

From the above parameters one can estimate the characteristic timescales for the CSO, seen in figure 24.

The timescales show us that high-energy protons can, and in any case will, under the right conditions, accelerate up to energies of $< 10^{20} \text{ eV}$. This limit is capped by the dynamical size of the emitting region and, of course, the magnetic field strength. The timescales also show us that the acceleration is dominated by synchrotron losses and photopion losses, and due to their small value, one would need to consider pair-pair losses as well, which is not done in this analysis. The lack of photopion loss dominance is a good sign for proton acceleration since it has been a limiting factor in other studies such as Peretti et al. 2023, where one has a higher luminosity object with processes happening even closer to the central engine. One can confirm the lack of photopion by comparing it to the work of Takami and Horiuchi 2011, which considered a young radio AGN with much bigger lobe sizes and much higher luminosity. In this case, the photopion losses are

Parameter	Value
L_d	10^{43} erg/s
GM	$G10^8 M_\odot$
RS	$\frac{2GM}{c^2}$
η	0.1
f_X	0.3
R_X	$30RS$
β	$0.4 c$
f_{BLR}	0.1
R_{BLR}	$10^{17} \sqrt{L_d/10^{45}}$ cm
f_{IR}	0.5
R_{IR}	$2.510^{18} \sqrt{L_d/10^{45}}$ cm
Γ	1.1

Table 7: Parameters used to determine the SED of the different regions.

Figure 24: Characteristic timescales for the CSO. Processes included is synchrotron losses and photopion losses. The timescales are calculated for a spherical size of $R_{lobe} = 2pc$ and a magnetic field strength of $B = 10^{-2}G$. The photon field is based on the parameters in table 7.

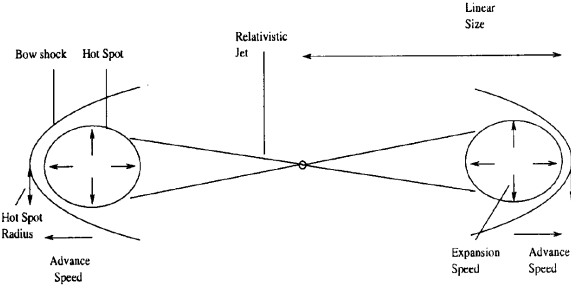


Figure 25: Schematic of the shock in the CSO. The shock is created by the expansion of the lobes into the ambient medium through jet pressure. Image taken from Perucho and Martí 2002

much higher than the synchrotron losses, and the acceleration is limited by the photopion losses. But one will note that Takami and Horiuchi 2011 did not consider the lifetime of the system, that is to say, the duration for which a CSO could maintain the shock structure that allows for acceleration, which I believe would severely limit the acceleration. The lack of photopion interaction will also be a limiting factor for neutrino production, something that will be discussed in the following sections.

Acceleration

From the above timescales, one can see that the maximum energy that can be obtained from the system via first-order Fermi acceleration is huge and significantly larger compared to second-order acceleration. For CSOs to remain candidates, it is clear that only first-order acceleration is possible, and therefore one will only consider this. One can justify that first-order acceleration happens in the hot spot due to the expansion of the lobes into the ambient medium. From radio observations, one has measured mildly relativistic expansion of the lobes, and with this comes naturally a shock boundary between the expanding hot spot and the ambient medium. This shock boundary produces a natural place for acceleration, and due to the compactness of CSOs, the downstream magnetic field is strong enough to allow for efficient acceleration. One can view the theoretical schematic of the shock in figure 25.

Second-order Fermi acceleration is not efficient in the CSO, which was to be expected. The acceleration is limited by the small size of the system, the low magnetic field strength, the too-high proton density, which leads to a low Alfvén wave speed, and more. One would need a substantial decrease in the diffusive acceleration timescale for second-order acceleration to be efficient. This is not the case in the CSO, and one can therefore conclude that the acceleration is dominated by first-order acceleration.

7.4 Composition/Mass Loading

A big problem in determining the viability of UHECRs and neutrino sources is the problem of ion density and composition. The available data obtained through radio measurements or other wavelengths are usually attributed to electrons.

7.4.1 Stellar Mass Loading

A mechanism for the deceleration of the jet in both CSO 2.0 and 2.1 stages is mass loading. That being the jet encountering various densities that supply an increase of mass to the jet, slowing it down sufficiently. In Sullivan et al. 2024, they find that the jet needs a mass loading rate of $0.2M_{\odot}\text{yr}^{-1}$ for 1000 years in order

to decelerate the jet sufficiently to explain the observed CSO 2.1 lifetimes. This loading rate can allow us to make simple estimates of the ion density that ends up in the lobes and that may experience acceleration.

For a given mass loading rate, one can assume an initial mass composition. By assuming that the mass loading is caused by stellar objects caught by the expanding jet, one can make some estimations. These objects will have a composition similar to the solar composition. The solar composition is 74% hydrogen, 24% helium, and 2% other elements. With this density, one can then estimate the number density of ions in the lobes assuming all mass loading ends up in the lobes via the following formula:

$$n_{\text{ions}} = \frac{0.2M_{\odot} \times 1000\text{yr}}{\frac{4}{3}\pi R_{\text{lobe}}^3 (74\%m_p + 24\%m_{\text{helium}} + 2\%m_{\text{heavier ions}})} \quad (71)$$

Setting $R = 10$ pc, a not unreasonable number for CSO 2.1, we get the number density of ions to be $n_{\text{ions}} = 2.9\text{cm}^{-3}$. This is not an unreasonably high number for the number density, and it is possible that the ion density is higher than this with part of the jet energy being carried by ions. From this estimate, one also receives the metallicity of the lobes, which is $Z = 0.02$, which is the solar metallicity. This as well is not an unreasonable number but is based on the assumption that the mass loading is caused by stellar objects.

Sullivan et al. 2024 find that the number of stars needed for the...

7.4.2 Metallicity

The metallicity of the lobes is also an unknown quantity.

7.5 Emissivity of the System

Based on the magnetic field strength, one can estimate the possible maximum energy achieved by a proton. In addition to this, one can estimate the number density of protons in the system through the mass loading rate and a composition by assuming it to be equal to that of solar masses. One also has the density of CSO sources to which this process is happening. With all this information and given a few assumptions on the energy spectra of the protons, one can estimate the emissivity of UHECRs from these sources.

The energy spectrum of protons undergoing first-order acceleration is usually a power law, but commonly one uses a broken power law to describe the spectrum. The spectrum of the number of protons per unit energy is given by:

$$N(\gamma) = \begin{cases} N_0\gamma^{-\alpha} & \gamma < \gamma_{\text{break}} \\ N_0\gamma_{\text{break}}^{-\alpha-1} & \gamma > \gamma_{\text{break}} \end{cases} \quad (72)$$

By arguing that the number of ions in the lobe is equal to the total mass loaded into the lobe, $V_{\text{lobe}}n_{\text{Ion}} = \int_{\gamma_{\text{min}}}^{\gamma_{\text{max}}} N(\gamma)d\gamma$, one can normalize the spectrum. In addition to this, one can separate the number of ions into those of different species by multiplying with the percentage of the mass that is of that species. With this, one can estimate the internal energy of any desired species in the lobe. γ_{max} can then be estimated based on the maximum energy of the particular species. The total internal energy of any species in the lobe can then be calculated as,

$$U_{\text{Ion}} = m_p c^2 \int_{\gamma_{\text{min}}}^{\gamma_{\text{max}}} \gamma N(\gamma)d\gamma \quad (73)$$

By assuming that all internal energy is converted to UHECRs and radiated away at a constant rate, one can estimate the luminosity of cosmic rays as $L_{\text{species}} = U_{\text{species}}/t_{\text{life}}$. One can separate the internal energy stored in all ions to those of the most energetic, that will become UHECRs by calculating the separate internal energy for UHECRs. That is to say, only ions with energy larger than $\gamma > 10^{10}$. By using our estimate of the density of CSO 2.0s at 10^{-5}Mpc^{-3} , $\gamma_{\text{max}} = 3 \times 10^{19} \times Z$ and $\gamma_{\text{min}} = 3$, one can estimate the emissivity of UHECRs per species as $Q_{\text{UHECR}} = L_{\text{species}} n_{\text{CSO}}$.

The results of the calculations can be seen in table 8.

Variable	Protons	Helium	Heavier Ions
$u (\text{erg cm}^{-3})$	8.284×10^{-12}	1.075×10^{-11}	6.045×10^{-12}
$L (\text{erg s}^{-1})$	1.020×10^{48}	1.323×10^{48}	7.440×10^{47}
$\epsilon (\text{erg Mpc}^{-3} \text{ yr}^{-1})$	3.858×10^{50}	5.005×10^{50}	2.815×10^{50}
$u_{\text{UHECRs}} (\text{erg cm}^{-3})$	4.692×10^{-29}	6.087×10^{-29}	3.424×10^{-29}
$L_{\text{UHECRs}} (\text{erg s}^{-1})$	5.774×10^{30}	7.491×10^{30}	4.214×10^{30}
$\epsilon_{\text{UHECRs}} (\text{erg Mpc}^{-3} \text{ yr}^{-1})$	2.185×10^{33}	2.835×10^{33}	1.595×10^{33}

Table 8: Mass Loading and Extra-Galactic Results for Different Species

7.6 Neutrino Emissivity

8 Discussion

References

- Aab, A. et al. (Sept. 2020). “Features of the Energy Spectrum of Cosmic Rays above 2.5 Using the Pierre Auger Observatory”. In: *Phys. Rev. Lett.* 125 (12), p. 121106. DOI: 10.1103/PhysRevLett.125.121106. URL: <https://link.aps.org/doi/10.1103/PhysRevLett.125.121106>.
- Abbasi, R. et al. (Mar. 2022). “Improved Characterization of the Astrophysical Muon–neutrino Flux with 9.5 Years of IceCube Data”. In: *The Astrophysical Journal* 928.1, p. 50. DOI: 10.3847/1538-4357/ac4d29. URL: <https://dx.doi.org/10.3847/1538-4357/ac4d29>.
- Abdul Halim, A. et al. (2023). “Constraining the sources of ultra-high-energy cosmic rays across and above the ankle with the spectrum and composition data measured at the Pierre Auger Observatory”. In: *Journal of Cosmology and Astroparticle Physics* 2023.05, p. 024. ISSN: 1475-7516. DOI: 10.1088/1475-7516/2023/05/024. URL: <http://dx.doi.org/10.1088/1475-7516/2023/05/024>.
- Abramowicz, Marek A. and Dr. Odele Straub (2023). *Accretion Discs*. 3.12.2023. URL: http://www.scholarpedia.org/article/Accretion_discs.
- Albers, Roland et al. (2024). “Magnetospheric Venus Space Explorers (MVSE) mission: A proposal for understanding the dynamics of induced magnetospheres”. In: *Acta Astronautica*. ISSN: 0094-5765. DOI: <https://doi.org/10.1016/j.actaastro.2024.05.017>. URL: <https://www.sciencedirect.com/science/article/pii/S0094576524002674>.
- Alves, E. P., J. Zrake, and F. Fiúza (Dec. 2018). “Efficient Nonthermal Particle Acceleration by the Kink Instability in Relativistic Jets”. In: *Physical Review Letters* 121.24. ISSN: 1079-7114. DOI: 10.1103/physrevlett.121.245101. URL: <http://dx.doi.org/10.1103/PhysRevLett.121.245101>.
- Alves Batista, Rafael et al. (June 2019). “Open Questions in Cosmic-Ray Research at Ultrahigh Energies”. In: *Frontiers in Astronomy and Space Sciences* 6. ISSN: 2296-987X. DOI: 10.3389/fspas.2019.00023. URL: <http://dx.doi.org/10.3389/fspas.2019.00023>.
- Andeen, Karen and Matthias Plum (Jan. 2019). “Latest Cosmic Ray Results from IceTop and IceCube”. In: *EPJ Web of Conferences* 210, p. 03005. DOI: 10.1051/epjconf/201921003005.
- Balasubramaniam, K. et al. (Nov. 2021). “X-Ray Emission of the gamma-ray-loud Young Radio Galaxy NGC 3894”. In: *The Astrophysical Journal* 922.1, p. 84. ISSN: 1538-4357. DOI: 10.3847/1538-4357/ac1ff5. URL: <http://dx.doi.org/10.3847/1538-4357/ac1ff5>.
- Bennun, Alfred (June 2020). “High Energy Dimensioning the Quantum Space-Time of the Electron”. In: Bian, Wei-Hao and Yong-Heng Zhao (June 2003). “Accretion Rates and the Accretion Efficiency in AGNs”. In: *Publications of the Astronomical Society of Japan* 55.3, pp. 599–603. ISSN: 0004-6264. DOI: 10.1093/pasj/55.3.599. eprint: <https://academic.oup.com/pasj/article-pdf/55/3/599/17447902/pasj55-0599.pdf>. URL: <https://doi.org/10.1093/pasj/55.3.599>.
- Blandford, R. D. and R. L. Znajek (July 1977). “Electromagnetic extraction of energy from Kerr black holes”. In: *Monthly Notices of the Royal Astronomical Society* 179.3, pp. 433–456. ISSN: 0035-8711. DOI: 10.1093/mnras/179.3.433. eprint: <https://academic.oup.com/mnras/article-pdf/179/3/433/9333653/mnras179-0433.pdf>. URL: <https://doi.org/10.1093/mnras/179.3.433>.
- Bronzini, E. et al. (2024). *Investigating X-ray Emission in the GeV-emitting Compact Symmetric Objects PKS 1718-649 and TXS 1146+596*. arXiv: 2401.16479 [astro-ph.HE].
- collaboration, The Pierre Auger (2013). “Bounds on the density of sources of ultra-high energy cosmic rays from the Pierre Auger Observatory”. In: *Journal of Cosmology and Astroparticle Physics* 2013.05, p. 009. DOI: 10.1088/1475-7516/2013/05/009. URL: <https://dx.doi.org/10.1088/1475-7516/2013/05/009>.
- Collaboration, The Pierre Auger et al. (2017). *The Pierre Auger Observatory: Contributions to the 35th International Cosmic Ray Conference (ICRC 2017)*. arXiv: 1708.06592 [astro-ph.HE].
- Collinson, James S. et al. (Oct. 2016). “Reaching the peak of the quasar spectral energy distribution – II. Exploring the accretion disc, dusty torus and host galaxy”. In: *Monthly Notices of the Royal Astronomical Society* 465.1, pp. 358–382. ISSN: 0035-8711. DOI: 10.1093/mnras/stw2666. eprint: <https://academic.oup.com/mnras/article-pdf/465/1/358/8593036/stw2666.pdf>. URL: <https://doi.org/10.1093/mnras/stw2666>.
- Dermer, Charlees D. and Govind Menon (2009). *High Energy Radiation from Black Holes: Gamma Rays, Cosmic Rays, and Neutrinos*. Princeton University Press.

- Dermer, Charles (Jan. 2001). "Maximum Particle Energies by Fermi Acceleration and the Origin of Cosmic Rays above the Knee". In:
- Fomalont, E. B. et al. (1996). *The VSOP 5 GHz Continuum Survey: The Pre-launch VLBA Observations*. National Radio Astronomy Observatory, Charlottesville, VA, USA; FÖMI Satellite Geodetic Observatory, Budapest, Hungary; Joint Institute for VLBI in Europe, Dwingeloo, The Netherlands; Physics and Astronomy Department, University of Calgary, Calgary, Alberta, Canada; Institute of Space and Astronautical Science, Sagamihara, Kanagawa, Japan. URL: <https://www.vlba.nrao.edu/astro/obsprep/sourcelist/6cm/>.
- Fox, Brendan (2008). *IceCube Neutrino Telescope, Astroparticle Physics at the South Pole*. Presentation. URL: <https://slideplayer.com/slide/14534323/>.
- George, M. R. et al. (July 2008). "On active galactic nuclei as sources of ultra-high energy cosmic rays". In: *Monthly Notices of the Royal Astronomical Society: Letters* 388.1, pp. L59–L63. ISSN: 1745-3925. DOI: 10.1111/j.1745-3933.2008.00499.x. eprint: https://academic.oup.com/mnrasl/article-pdf/388/1/L59/54682864/mnrasl_388_1_159.pdf. URL: <https://doi.org/10.1111/j.1745-3933.2008.00499.x>.
- Ghisellini, G. and F. Tavecchio (Aug. 2009). "Canonical high-power blazars". In: *Monthly Notices of the Royal Astronomical Society* 397.2, pp. 985–1002. ISSN: 1365-2966. DOI: 10.1111/j.1365-2966.2009.15007.x. URL: <http://dx.doi.org/10.1111/j.1365-2966.2009.15007.x>.
- Hillas, A. M. (1984). "The Origin of Ultra-High-Energy Cosmic Rays". In: *Annual Review of Astronomy and Astrophysics* 22.1, pp. 425–444. DOI: 10.1146/annurev.aa.22.090184.002233. URL: <https://doi.org/10.1146/annurev.aa.22.090184.002233>.
- Hirotani, Kouichi (Jan. 2005). "Kinetic Luminosity and Composition of Active Galactic Nuclei Jets". In: *The Astrophysical Journal* 619.1, pp. 73–85. ISSN: 1538-4357. DOI: 10.1086/426497. URL: <http://dx.doi.org/10.1086/426497>.
- Hogg, David W. (2000). *Distance measures in cosmology*. arXiv: astro-ph/9905116 [astro-ph].
- Jacobsen, Idunn B. et al. (2015). "High-energy neutrino fluxes from AGN populations inferred from X-ray surveys". In: *Mon. Not. Roy. Astron. Soc.* 451.4, pp. 3649–3663. DOI: 10.1093/mnras/stv1196. arXiv: 1506.05916 [astro-ph.HE].
- Kiehlmann, S., M. L. Lister, et al. (2023). *Compact Symmetric Objects – I Towards a Comprehensive Bona Fide Catalog*. arXiv: 2303.11357 [astro-ph.HE].
- Kiehlmann, S., A. C. S. Readhead, et al. (2023). *Compact Symmetric Objects – II Confirmation of a Distinct Population of High-Luminosity Jetted Active Galaxies*. arXiv: 2303.11359 [astro-ph.HE].
- Marscher, A. P. (1983). "Accurate formula for the self-Compton X-ray flux density from a uniform, spherical, compact radio source." In: *apj* 264, pp. 296–297. DOI: 10.1086/160597.
- Mason, Rachel E (2015). "Dust in the torus of the AGN unified model". In: *Planetary and Space Science* 116. Cosmic Dust VII, pp. 97–101. ISSN: 0032-0633. DOI: <https://doi.org/10.1016/j.pss.2015.02.013>. URL: <https://www.sciencedirect.com/science/article/pii/S0032063315000483>.
- Netzer, Hagai (2015). "Revisiting the Unified Model of Active Galactic Nuclei". In: *Annual Review of Astronomy and Astrophysics* 53.1, pp. 365–408. DOI: 10.1146/annurev-astro-082214-122302. URL: <https://doi.org/10.1146/2Fannurev-astro-082214-122302>.
- O'Sullivan, S., B. Reville, and A. M. Taylor (Nov. 2009). "Stochastic particle acceleration in the lobes of giant radio galaxies". In: *Monthly Notices of the Royal Astronomical Society* 400.1, pp. 248–257. ISSN: 1365-2966. DOI: 10.1111/j.1365-2966.2009.15442.x. URL: <http://dx.doi.org/10.1111/j.1365-2966.2009.15442.x>.
- Orienti, M. and D. Dallacasa (Dec. 2013). "Physical properties of young radio sources: VLBA observations of high-frequency peaking radio sources". In: *Monthly Notices of the Royal Astronomical Society* 438.1, pp. 463–475. ISSN: 0035-8711. DOI: 10.1093/mnras/stt2217. eprint: <https://academic.oup.com/mnras/article-pdf/438/1/463/18463416/stt2217.pdf>. URL: <https://doi.org/10.1093/mnras/stt2217>.
- Peretti, Enrico et al. (2023). *Diffusive shock acceleration at EeV and associated multimessenger flux from ultra-fast outflows driven by Active Galactic Nuclei*. arXiv: 2301.13689 [astro-ph.HE].
- Perucho, M. and J. M. Martí (Apr. 2002). "Physical Parameters in the Hot Spots and Jets of Compact Symmetric Objects". In: *The Astrophysical Journal* 568.2, pp. 639–650. ISSN: 1538-4357. DOI: 10.1086/338882. URL: <http://dx.doi.org/10.1086/338882>.

- Readhead, A. C. S. et al. (2023). *Compact Symmetric Objects – III Evolution of the High-Luminosity Branch and a Possible Connection with Tidal Disruption Events*. arXiv: 2303.11361 [astro-ph.HE].
- Sanders, Nathan (2021). *Guide to Classification of Galaxies and AGNs*. 15.11.2023. URL: <https://astrobites.org/guides/galaxy-and-agn-types/>.
- Shields, Gregory A. (1999). “A Brief History of Active Galactic Nuclei”. In: *Publications of the Astronomical Society of the Pacific* 111.760, pp. 661–678. DOI: 10.1086/316378. URL: <https://doi.org/10.1086/2F316378>.
- Stanev, Todor (June 2009). “Propagation of ultrahigh-energy cosmic rays”. In: *New Journal of Physics* 11.6, p. 065013. DOI: 10.1088/1367-2630/11/6/065013. URL: <https://dx.doi.org/10.1088/1367-2630/11/6/065013>.
- Sullivan, Andrew G. et al. (2024). *Small-scale radio jets and tidal disruption events: A theory of high-luminosity compact symmetric objects*. arXiv: 2401.14399 [astro-ph.HE].
- Takami, Hajime and Shunsaku Horiuchi (2011). “The production of ultra high energy cosmic rays during the early epochs of radio-loud AGN”. In: *Astroparticle Physics* 34.10, pp. 749–754. ISSN: 0927-6505. DOI: <https://doi.org/10.1016/j.astropartphys.2011.01.014>. URL: <https://www.sciencedirect.com/science/article/pii/S0927650511000272>.
- Tremblay, S. E. et al. (Mar. 2016). “Compact symmetric objects and supermassive binary black holes in the VLBA Imaging and Polarimetry Survey”. In: *Monthly Notices of the Royal Astronomical Society* 459.1, pp. 820–840. ISSN: 1365-2966. DOI: 10.1093/mnras/stw592. URL: <http://dx.doi.org/10.1093/mnras/stw592>.
- Walg, S. et al. (June 2013). “Relativistic AGN jets I. The delicate interplay between jet structure, cocoon morphology and jet-head propagation”. In: *Monthly Notices of the Royal Astronomical Society* 433.2, pp. 1453–1478. ISSN: 0035-8711. DOI: 10.1093/mnras/stt823. eprint: <https://academic.oup.com/mnras/article-pdf/433/2/1453/4923906/stt823.pdf>. URL: <https://doi.org/10.1093/mnras/stt823>.
- Wilson, Thomas L., Kristen Rohlfs, and Susanne Hüttemeister (2013). *Tools of Radio Astronomy*. DOI: 10.1007/978-3-642-39950-3.
- Wójtowicz, A. et al. (Apr. 2020). “On the Jet Production Efficiency in a Sample of the Youngest Radio Galaxies”. In: *The Astrophysical Journal* 892.2, p. 116. ISSN: 1538-4357. DOI: 10.3847/1538-4357/ab7930. URL: <http://dx.doi.org/10.3847/1538-4357/ab7930>.